EUMETSAT Satellite Application Facility on

Support to Operational Hydrology and Water Management

Algorithm Theoretical Baseline Document (ATBD)

for product P-IN-MHS (H02B)

P-IN-MHS - Precipitation rate at ground by MW cross-track scanners

Reference Number:	SAF/HSAF/ATBD-02B
Issue/Revision Index:	1.2
Last Change:	01 March 2019

DOCUMENT CHANGE RECORD

Issue / Revision	Date	Description
1.0	02/03/2015	Baseline version prepared for PCR
1.1	02/12/2015	Version prepared for PCR close-out which acknowledges the outcomes of the review. Following changes applied: Area coverage specified (answer to RID 001) Validation strategy updated in section 3.3.9 (answer to RID 002) Performances information updated in Section 3.3.6 (answer to RID 006) Section 1.2 revised (answer to RID 016) Section 2.1 improved: description of CDRD approach added (answer to RID 020), stratiform distinction clarified (answer to RID 022), GHz of MHS Channels corrected (answer to RID 021)
1.2	01/03/2019	Updated version submitted to delta ORR, which acknowledges the RIDs from ORR full disc

INDEX

Purpose of this document 6
1 Introduction to product P-IN-MHS 7
1.1 Sensing principle 7
1.2 Main operational characteristics 8
1.3 Architecture of the products generation chain 9
2 Processing concept 10
2.1 Basic principles 10
2.2 Introduction to the AMSU/MHS processing chains 11
3 Algorithm description 12
3.1 Brightness Temperature Preprocessing 12
3.2 Precipitation screening 14
3.3 The Precipitation Retrieval Algorithm 16
3.3.1 The neural network approach 16
3.3.2 Training the ANN by CRM simulations 17
3.3.3 The UW-NMS Cloud Resolving Model 22
3.3.4 The Radiative Transfer Model 26
3.3.5 The Instrument model 28
3.3.6 The neural network 29
3.3.7 Assumptions and limitations 32
3.3.8 Quality Index and phase flag 33
3.3.9 The quality index 34
3.3.10 Algorithm validation/heritage 36
4 Examples of P-IN-MHS product 37
5 References 38
Annex 1: Introduction to H SAF 43
The EUMETSAT Satellite Application Facilities 43
Purpose of the H SAF 44
Products / Deliveries of the H SAF 45
System Overview 45
Annex 2: Acronyms 46

List of Tables

Table 01	AMSU-A and MHS channel description (AMSU-B channel characteristics are also provided).	
Table 02	Data used in limb-and-surface correction of AMSU-A channels	17
Table 03	List of CCA coefficients and mean TB values used by the precipitation screening algorithm for Arid Land (desert)	19
Table 04	List of all simulations used to generate the African database for H02B	23
Table 05	Channels utilized by the PNPR algorithm	29
Table 06	ANN synthetic performances for different background surfaces	31
Table 07	Phase flag values and interpretation	34
Table 08	Quality index values and interpretation and correspondence with percentage of confidence index (PCI)	35
Table 09	Preliminary PCI thresholds based on screening algorithm	35
Table 10	Preliminary PCI based on precipitation type	35

List of Figures

Fig. 01	Viewing geometry of cross-track scanning radiometer AMSU-A	11
Fig. 02	Coverage of the H SAF area by the NOAA-18 MHS in one day. Channel 89 GHz, V polarisation, 23-24 Apr 2017. In each panel the orbit sequence is from right to left.	
Fig. 03	Architecture of the H02B production chain architecture	
Fig. 04	Flow chart of the AMSU-MHS precipitation rate processing chain	15
Fig. 05	NOAA-18 AMSU-A 53.6-GHz brightness temperatures for a northbound track on 06 July 2010. (a) Uncorrected, and (b) Limb-and-surface corrected	17
Fig. 06	Map of areas identified as desert or arid land	19
Fig. 07	A 2-layer feed forward neural net with one output node	20
Fig. 08	Inner domains of the 60 NMS simulations over the H SAF area, divided by season	21
Fig. 09	Climatic regions identified over the African continent and represented in the database used in H02B	22
Fig. 10	Example of a TRMM PR overpass over Africa at 02:36 UTC on 02/07/2008 and detail of the area affected by the precipitation with PR derived Rainfall rate (mm/h), Freezing level height (m) and rain type	23
Fig. 11	Spatial distribution of the Inner domain of the 34 NMS simulations over the African region for the H02B training database	25
Fig. 12	Flow diagram of the H02B algorithm	33
Fig. 13	Example of phase flag for a case study over Italy. Left: Phase of precipitation; right: retrieved precipitation [mm/h]; - NOAA 18 - 10 February 2012 13:27 UTC	34

Fig. 14 Example of a 157 GHz image for MHS orbit over the MSG area LAT 60°S - 75°N, LON 60°W - 60°E (left panel) and H02B rainfall rate (mm/h) (right panel) - MetOp-A - 06 January 2012, 18:09 UTC 37

Fig. 15 Example of H02B PCI (left panel) and Phase flag (right panel) [0 no data, 1 liquid, 2 solid, 3 mixed]- MetOp-A - 06 January 2012, 18:09 UTC 37

Purpose of this document

This document describes the algorithm used to deliver H SAF H02B product (acronym P-IN-MHS: <Precipitation product> - <Instantaneous precipitation rate> – <Orbital> – <Neural Network based> – <AMSU/MHS>) and provides some details on the operating scheme, the physical approach and the output variables and flags provided to the final user.

P-IN-MHS is based on a neural network approach and provides precipitation rate estimates from the Advanced Microwave Sounding Unit-A (AMSU-A) and the Microwave Humidity Sounder (MHS) observations [please, note that the Advanced Microwave Sounding Unit-B (AMSU-B) available on NOAA 15 and NOAA 16 is no longer available]. The algorithm optimally exploits the different characteristics of AMSU/MHS channels, and their combinations, including the brightness temperature (TB) differences of the 183.31 GHz channels, with the goal of having a single neural network for different types of background surfaces. The training of the neural network is based on the use of a cloud-radiation database, built from cloud-resolving model simulations coupled to a radiative transfer model, representative of the European and African precipitation climatology (LAT 60°S - 75°N, LON 60°W - 60°E).

The algorithm provides the surface precipitation rate (mm/h), the phase of the precipitation, and a pixel-based confidence index for the evaluation of the reliability of the retrieval.

1 Introduction to product P-IN-MHS

1.1 Sensing principle

The product P-IN-MHS is based on the instruments AMSU-A and MHS flown on NOAA and MetOp satellites. These cross-track scanners provide images with constant angular sampling across track, that implies that the instantaneous field of view (IFOV) elongates as the beam moves from nadir toward the edge of the scan (see ***Fig. 01***).

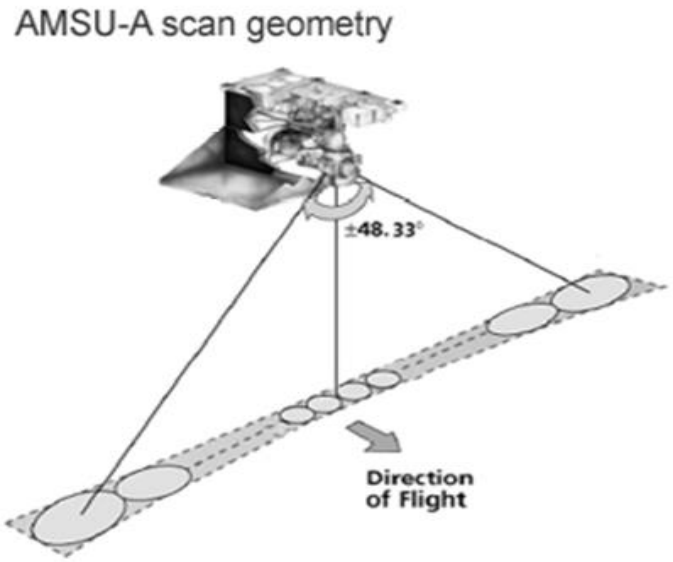

Fig. 01 Viewing geometry of cross-track scanning radiometer AMSU-A

The fifteen channel frequencies of the AMSU-A instrument are 23.8, 31.4, 50.3, 52.8, 53.6, 54.4, 54.94, 55.5, 57.29, 5@57.29±Δ*F*±Δ*f* and 89 GHz (where ±Δ*F*±Δ*f* represents either double or quadruple symmetric sideband frequency positions along the 57.29 GHz O_2 line's wing -- necessary for temperature sounding), while the five frequencies of the MHS radiometer are 89, 157, 183.31±1, 183.31±3 and 183.31±7 GHz (see **Table 01**, where AMSU-B characteristics are also shown for comparison). This information is accessible in more detail from AMSU-A (2009) and MHS (2009) documents.

Table 01 – AMSU-A and MHS channel description (AMSU-B channel characteristics are also provided).

	AMSU-A	MHS
Host Satellite [nominal satellite height]		
1	NOAA-18/19 POES [833 km]	NOAA-18/19 POES [833 km]
2	METOP-A/B [817 km]	METOP-A/B [817 km]
Frequency (GHz) / Pol. State @ Nadir		
1	23.8 / R : V	89 / R : V
2	31.4 / R : V	157 / R : V
3	50.3 / R : V	183.311±1 / R : H
4	52.8 / R : V	183.311±3 / R : H
5	53.596±0.115 / R : H	183.311±7 / R : V
6	54.4 / R : H	

7	54.94 / R : V	**AMSU-B**
8	55.5 / R : H	**Host Satellite [nominal satellite height]**
9	57.29 / R : H	Pre-NOAA-18 POES Platforms [833 km]
10	57.29±0.217 / R : H	**Frequency / Pol. State @ Nadir**
11	57.29±0.3222±0.048 / R : H	89±0.9 / R : V
12	57.29±0.3222±0.022 / R : H	150±0.9 / R : V
13	57.29±0.3222±0.01 / R : H	183.31±1 / R : V
14	57.29±0.3222±0.0045 / R : H	183.31±3 / R : V
15	89 / R : V	183.31±7 / R : V

The IFOV resolutions / shapes are a function of the radiometer, the view angle and the height of the satellite, where shape is expressed in terms of cross-track (CT) and down-track (DT) elliptic dimensions. Both the AMSU-A and MHS radiometers use their own common beam sizes, specific to each radiometer, unvarying with respect to channel frequency, *i.e.*, the IFOV resolutions are independent of the frequency dependent diffraction limits. For example, for the AMSU-A radiometer at a nominal satellite height of 833 km, the nadir and scan edge IFOV resolutions/shapes, respectively, are 49.33-CT x 48.17-DT km^2/near-circular and 179.89-CT x 80.8-DT km^2/extreme-ovate, while for the MHS radiometer at the same satellite height, the nadir and scan edge IFOV resolutions/shapes, respectively, are 20.36-CT x 16.59-DT km^2/mild-ovate and 67.14-CT x 27.91-DT km^2/extreme-ovate.

Since the incidence angle changes moving cross-track, the effect of polarisation also changes, thus the information stemming from dual polarisation would be very difficult to be used, and in effect the various frequencies are observed under a single polarisation, V or H.

The NOAA satellites are managed by NOAA, MetOp by EUMETSAT. Both NOAA and MetOp provide direct-read-out (the real-time transmitter of MetOp suffered of a failure, but now transmission of data over Europe has been resumed).

1.2 Main operational characteristics

The horizontal resolution (Δx). Lower resolution AMSU-A data are resampled over the AMSU-B/MHS grid by means of bilinear interpolation. The product resolution corresponds approximately to the nominal resolution of MHS, varying with the viewing scan angle from 16 x 16 km^2 / circular at nadir to 26 x 52 km^2/ovate at scan edge. The sampling distance also varies with viewing scan angle and corresponds to the sampling geometry of MHS (1.1 degrees), which corresponds to 16 km at nadir.

The *observing cycle (Δt)*. NOAA-18 and NOAA-19, follow approximately the same orbit, close to 14:00 local solar time (LST). MetOp has LST around 9:30. In average the observing cycle over Europe is $\Delta t \sim$ 6 h, with actual interval ranging from 4.5 to 7.5 hours. Gaps are filled by other H SAF precipitation products developed for other MW radiometers. For example, P-IN-SSMIS for SSMIS, has observing cycle $\Delta t \sim$ 5 h, but LST around 7:00 and 18:00, with actual intervals ranging from 2 to 7 hours. The conclusion is:

- For P-IN-MHS as standalone (from NOAA & MetOp satellites): cycle Δt = 6 h, but it changes with latitude. Sampling 4.5÷7.5 h;

The *timeliness (δ)*. Direct-read-out is provided by all NOAA and MetOp satellites and, after partial recovery from the Advanced High Resolution Picture Transmission System (AHRPT) transmitter failure, also by MetOp-A. After adding the processing time we have:

- Timeliness $\delta \sim$ 0.5 h.

The *accuracy* is evaluated *a-posteriori* by means of the validation activity.

Spatial coverage:
The P-IN-MHS product has been designed to operate over the MSG Full disk geographical area (**Fig. 02**) (LAT 60°S - 75°N, LON 60°W - 60°E).

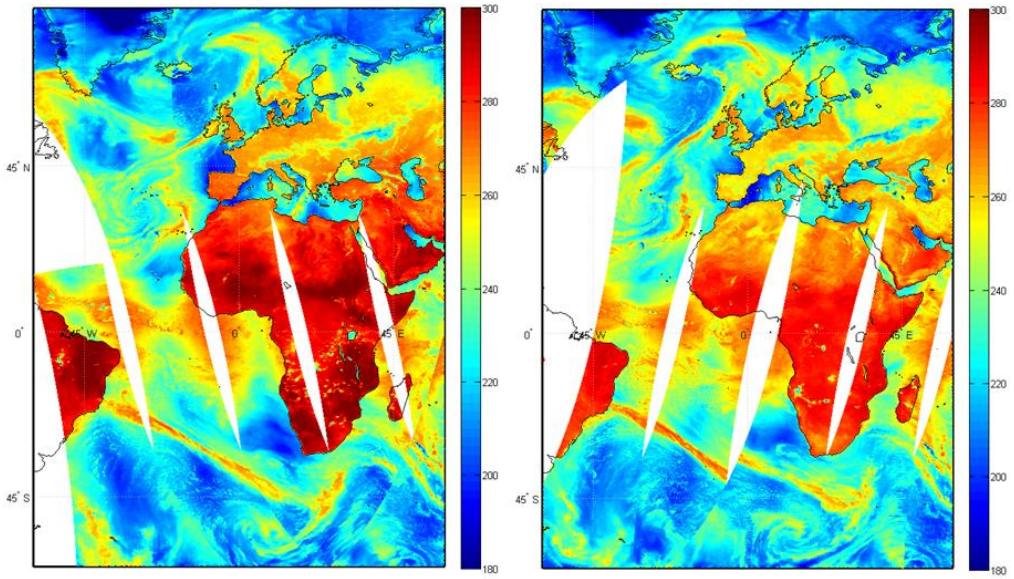

Fig. 02- Coverage of the H SAF area by the NOAA-18 MHS in one day. Channel 89 GHz, V polarisation, 23-24 Apr 2017. In each panel the orbit sequence is from right to left.

1.3 Architecture of the products generation chain

The architecture of the H02 (A and B) product generation chain is shown in ***Fig. 03***.

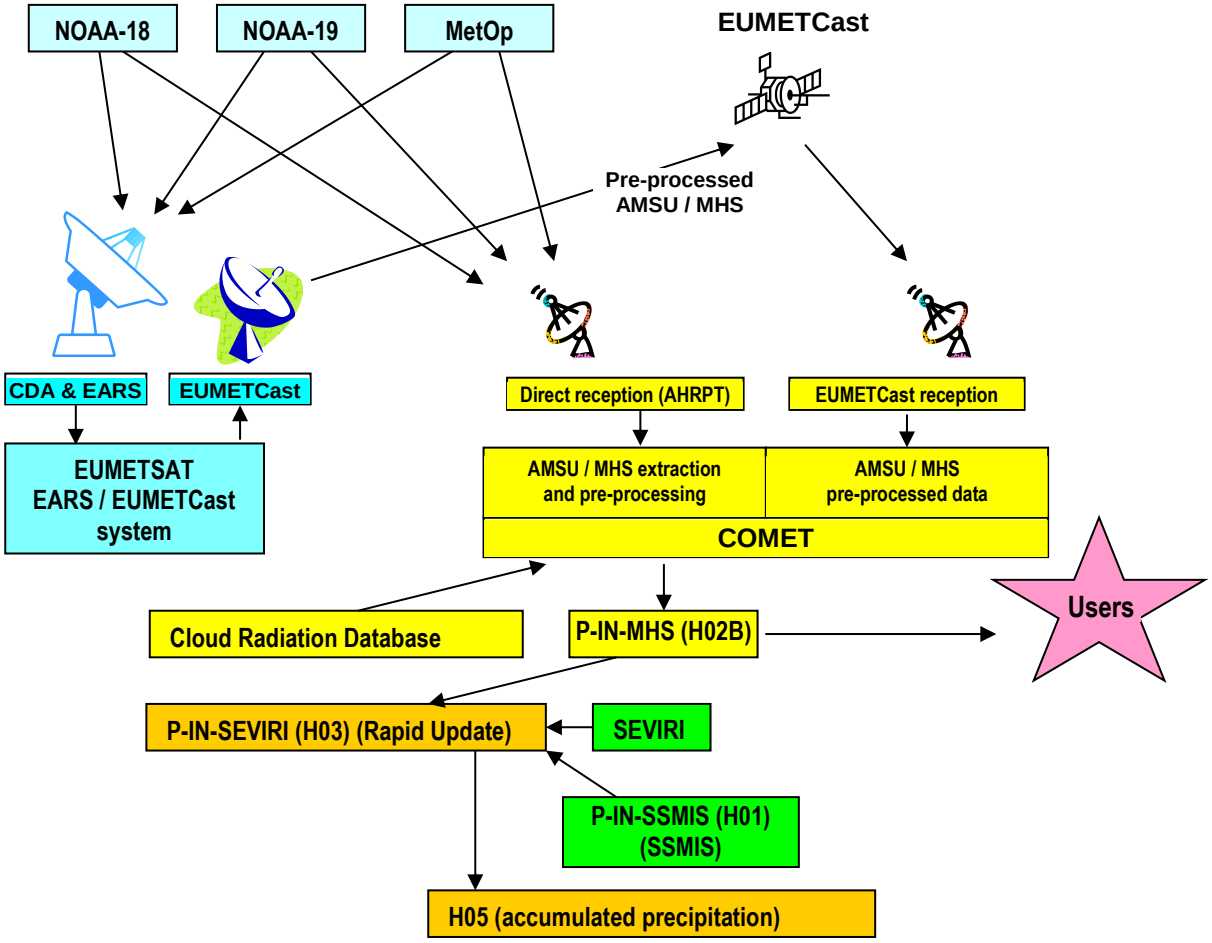

Fig. 03- Architecture of the H02 (A and B) production chain.

A main feature of the architecture of P-IN-MHS is the availability of direct read out through the AHRPT, and the alternative acquisition scheme through the EARS/EUMETCast system to cover in near-real-time the areas outside the acquisition range of the Rome AHRPT station.

The figure shows that the P-IN-MHS product, in addition to be disseminated to the users, is also used internally to COMET to feed the blended MW/IR Rapid-Update product (P-IN-SEVIRI - H03).

In COMET, the P-IN-MHS product is generated on the base of the algorithms and the databases developed and provided by CNR-ISAC.

The product, that includes some online quality control information, is disseminated to the Users by FTP.

2 Processing concept

2.1 Basic principles

Product P-IN-MHS is fundamentally based on AMSU-A and MHS instruments. These instruments are primarily designed for temperature (AMSU-A) and humidity (MHS) profiles, not specifically for precipitation. However, they are usefully exploited for precipitation retrieval. As cross-track scanners, they provide images with variable zenith angle, implying different optical path in the atmosphere and not homogeneous impact of the polarisation effects. Moreover, cross-track scanning provides variable

resolution across the scan. Another aspect to be considered is the large IFOV of low frequency AMSU-A channels.

The use of physically-based Bayesian algorithms for cross-track scanning microwave radiometers may be quite lengthy and cumbersome, due to the changing direction of view that implies direction-dependent fields of view, polarizations, and optical paths. Thus, for such radiometers it is more convenient relying on the use of artificial neural network (ANN) algorithms that implicitly solve such problems. The H SAF P-IN-MHS is based on the neural network algorithm of the ISAC-Rome called Passive Microwave Neural-network Precipitation Retrieval algorithm (PNPR) described in detail by Sanò et al. (2015). The algorithm was inspired by the investigations of Surussavadee and Staelin (2008a, b), whose approach was used for the previous versions of H02 (see Section 4.4). Origins and motivations for the development of PNPR are described in Mugnai et al. (2013b).

The new version of PNPR used for P-IN-MHS is based on a new optimal three-layer ANN which has derived its training database from the same Cloud Resolving Model (CRM) simulations and the same radiative transfer equation (RTE) model that are used for P-IN-SSMIS product for the SSMIS radiometers on board the U.S. Defense Meteorological Satellite Program (DMSP) satellites (based on the Bayesian Cloud Dynamics and Radiation Database - CDRD - algorithm).

The CDRD Algorithm is based on the extension of the Cloud Radiation Database (CRD) method by incorporating an extensive mix of the Cloud Resolving Model dynamical, thermodynamical, hydrometeorological, and microphysical variables. The original idea has been developed within the H SAF project and described in several recent papers (Sanò et al., 2013, Casella et al., 2012, 2013, Mugnai et al., 2013b, Smith et al., 2013).

H SAF seeks to support precipitation algorithms for cross-track scanning radiometers as consistent as possible with those for conically scanning radiometers, as well as precipitation algorithms optimized for the area of interest, i.e., the European / Mediterranean basin region, Africa, and Southern Atlantic. To have these two H SAF passive microwave (PMW) products based on the same physical foundation (same cloud model simulations, microphysics parameterization, and radiative transfer model), is a first necessary condition to achieve consistency of precipitation retrievals from cross-track and conical scanning radiometers for the same event. This consistency, besides the accuracy of the retrievals, is necessary in order to be able to fully exploit all cross-track and conical scanning radiometer overpasses for a specific event (available at about 3 hour time interval), and to be able to use both algorithms for monitoring precipitation at higher spatial/temporal resolution (i.e., blending techniques with IR observations), as well as for nowcasting and/or hydrological applications.

2.2 Introduction to the AMSU/MHS processing chains

As mentioned is Section 3.1, we intend to implement advanced processing for AMSU-A and MHS in respect of current practise. ***Fig. 04*** shows the flow chart of the processing chain.

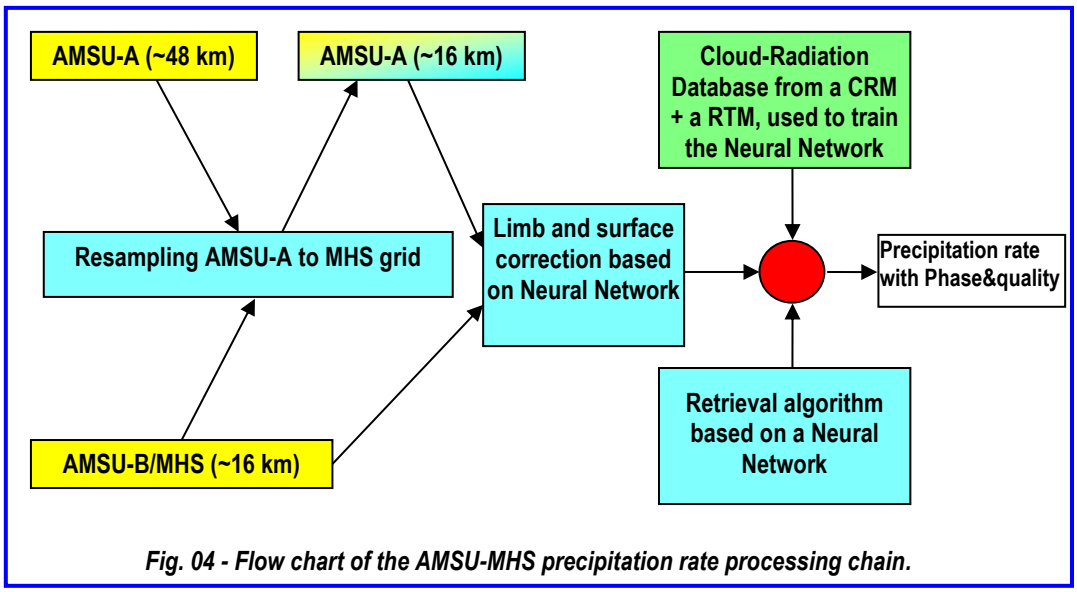

Fig. 04 - Flow chart of the AMSU-MHS precipitation rate processing chain.

The first step is to resample AMSU-A brightness temperature to MHS grid using bilinear interpolation. Then AMSU-A and MHS radiometers are corrected for limb and surface effects, to report the viewing geometry changing across the image to vertical viewing. This is obtained by applying procedures based on specific neural networks (one network for each channel). The corrected TBs are then used as input to the ANN-based retrieval algorithm to retrieve the instantaneous rain field.

3 Algorithm description

The following Sections describe the algorithms used in the various modules of the precipitation products generation chain. The degree of detail is consistent with the requirement of a manageable document. For further details please refer to Sanò et al. (2015) for the Neural Network algorithm description and to Panegrossi et al. (2014) for the extension of the algorithm to Africa and Southern Atlantic.

3.1 Brightness Temperature Preprocessing

This section describes the signal processing components which process AMSU data into forms that characterize information about the degrees of freedom most relevant to precipitation rate. An effort has been made to make the inputs to the neural net as insensitive to surface variations as possible so that the algorithm can be applied over land and sea.

AMSU observes at angles up to about 49 degrees away from nadir. For angles further away from nadir, electromagnetic energy originating from a given altitude and atmospheric state would have to travel longer paths before reaching the radiometer and, therefore, would be subject to more absorption and scattering effects. This results in scan-angle dependent effects in brightness temperature images: up to 30 K for 23.8 GHz, and up to 15 K for sounding channels (53-58 GHz).

Adjusting the so called “limb effects” is a common task at NOAA (Wark 1993) and it is fundamental for most of the use of sensors data. It is quite obvious that regression retrievals not adjusted to a common view angle will probably suffer from spot-to-spot systematic errors if the temporal distribution and sample size of the collocated data, as function of the beam position, vary considerably.

Even if physical retrieval algorithms often retrieve along the optical path, generally some sort of beam position-dependent bias adjustment is needed to remove spot-to-spot systematic biases caused by asymmetry of the observations.

If the limb adjustment procedure produces accurate limb-adjusted data, then also a physical retrieval will be simplified since there would be no need for spot dependent bias adjustment. Moreover, averaging satellite observations to a given grid map requires the data are limb-adjusted prior to averaging. Otherwise the data averaged will be associated with different atmospheric weighting functions.

At the beginning (Wark 1993), the Limb-and-Surface correction was implemented in a pure statistical manner for the operational use of TIROS satellite data. Goldberg et al. (1995) proposed instead a physical approach aiming at climate change monitoring in which one solves for coefficients that combine weighting functions from the off-nadir position to best fit the nadir weighting functions. More recently NOAA merged the two approaches in Goldberg et al. (2001), where the physical coefficients are used as a constraint in the Wark (1993) statistical approach.

We prefer to use the Chen (2004) ANN approach where the limb-and-surface correction is obtained by training neural networks to estimate nadir-viewing TB. The ANN uses TBs in the pixel to estimate TB seen at the pixel closest to nadir at a nearly identical latitude and at nearly the same time (see ***Table 02*** for inputs needed to correct AMSU-A channels 4-8).

It is worth pointing out that the ANN designed to reduce the limb effect of the AMSU-A oxygen absorption band channels (around 50 GHz), used to correct the 53.6 GHz channel in the screening procedure (Section 3.2), is different from the ANN designed to retrieve the surface precipitation. Note that AMSU-A channels 9-14 brightness temperatures are not corrected because they are not significantly perturbed by clouds and therefore are not used in the retrieval. It is also assumed that the high frequency channels (AMSU-B/MHS channels) do not require a dedicated procedure to correct the limb effect which is handled (learned/corrected) directly by the ANN used in the retrieval process.

Table 02 - Data used in limb-and-surface correction of AMSU-A channels

AMSU-A Channel	Inputs used for limb-and-surface correction
4	AMSU-A channels 4-12, land/sea flag, cos**θ**
5	AMSU-A channels 4-12, land/sea flag, cos**θ**
6	AMSU-A channels 6-12, cos**θ**
7	AMSU-A channels 6-12, cos**θ**
8	AMSU-A channels 6-12, cos**θ**

The limb correction ANNs were trained using data between 55°N and 55°S from seven orbits spaced over one year. Channels 4 and 5 are surface sensitive, so they were trained to estimate brightness temperatures that would be seen over land. The training data included brightness temperatures simulated (Mesoscale Model-5 (MM5) described by Dudhia (1993) and Grell et al. (1994)) for several storms at nadir and at all satellite zenith angles. ***Fig. 05*** shows one example of obtained results.

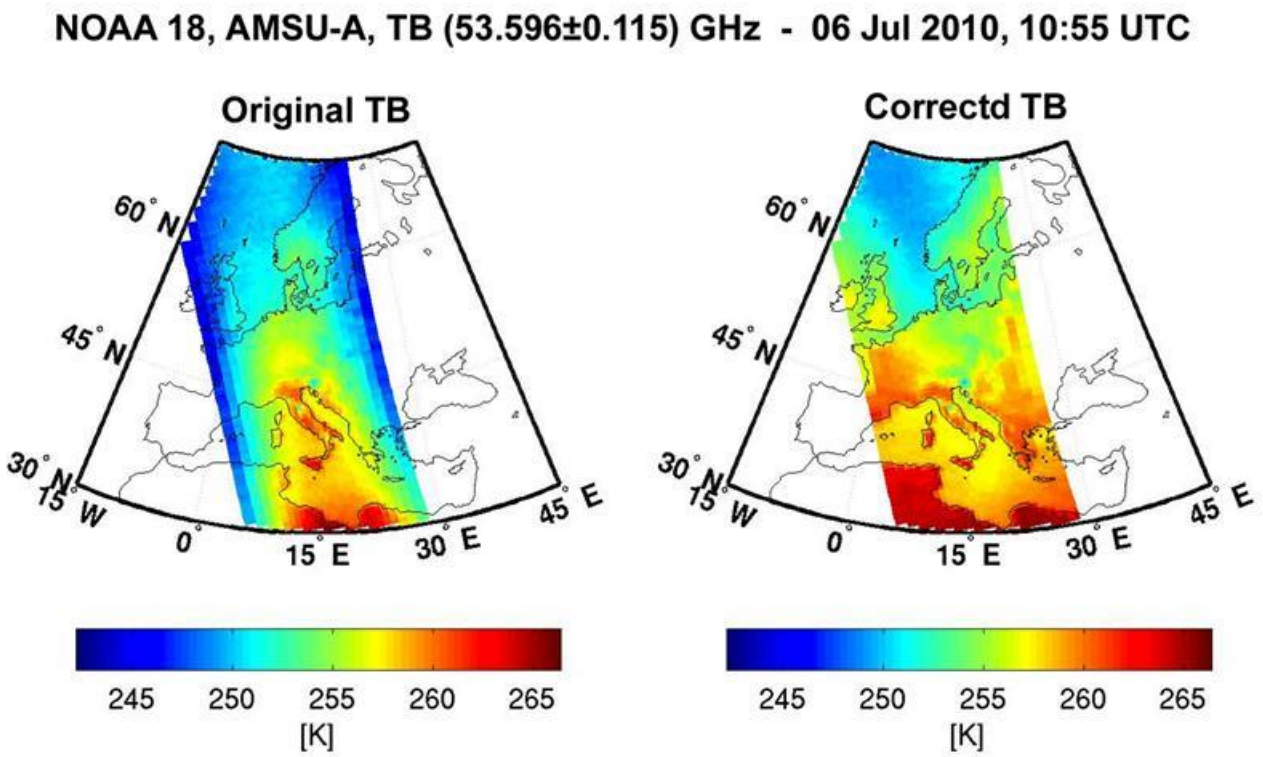

Fig. 05 - NOAA-18 AMSU-A 53.6-GHz brightness temperatures for a northbound track on 06 July 2010. (a) Uncorrected, and (b) Limb-and-surface corrected

3.2 Precipitation screening

The PNPR precipitation rate retrieval algorithm, designed for the H SAF P-IN-MHS product, has as first task the identification of potentially precipitating pixels. Channels used for this purpose should be sensitive to precipitation but should not exhibit large angle-dependent variations and surface variations.

Unprocessed brightness temperatures from AMSU-A channels 4-14 are not used directly because they exhibit excessive angle-dependent variations or have weighting functions that peak far above the range of altitudes in which most precipitation exists. AMSU-A channels 1, 2, 3, and 15, and the MHS 89.0-GHz and 157-GHz channels were not used because of their sensitivity to surface variations. The MHS channels ordered by opacity are as follows: 89 GHz (most transparent), 157 GHz, 183±7 GHz, 183±3 GHz, and 183±1 GHz (most opaque). The 183±7 GHz channel is sensitive to precipitation but does not show excessive surface variations. The 183±7 GHz channel is reasonably good for detecting precipitation also because the angle-dependent variation of precipitation-free brightness temperatures is small when compared to the variation due to precipitation.

Over all background surfaces except over desert the screening of not-precipitating pixels is based on the methodology described in Mugnai et al. (2013b). All 15-km pixels with brightness temperatures at 183±7 GHz that are below a threshold T7 are flagged as potentially precipitating, where

$T_7 = 0.667\ (T^{max}_{53.6} - 248) + 252 + 6 \cos\theta$

and where ϑ is the satellite zenith angle and $T^{max}_{53.6}$ is the spatially filtered limb-corrected 53.6 GHz brightness temperature obtained by selecting the warmest brightness temperature within a 7×7 array

of MHS pixels. It has been seen that the threshold T_7 can vary with atmospheric temperature. This threshold was determined empirically.

However, the 183±7 GHz channel can become sensitive to surface variations in very cold, dry atmospheric conditions. When $TB_{53.6}$ is less than 248 K, the 183±3 GHz brightness temperature is compared to a threshold T_3

$T_3 = 242.5 + 5 \cos \theta$.

In that case, if $TB_{183\pm3}$ is less than T_3, the pixel is flagged as potentially precipitating. The thresholds T_7 and T_3 are slightly colder than a saturated atmosphere would be, implying the presence of a microwave-absorbing or scattering cloud. It is possible for the 183±3 GHz and the 183±1 GHz channels to be sensitive to surface variations. If $TB_{53.6}$ is less than 242 K, then the pixel is assumed not to be precipitating.

Over desert (or arid land) the screening of not-precipitating pixels is based on the methodology developed by Casella et al. (2015). The Arid Land pixels have been identified looking at the mean annual difference of the DMSP SSMIS 19 GHz V and H channels. (Grody, 1991) has shown how the difference of the V and H polarized channels are very effective in identifying desert. Although the presence of clouds may reduce the polarization difference, this effect may be minimized by averaging the TB difference over a long period. One year (2011) of SSMIS observations over the area of interest has been used, selecting the observations over land, and remapping them on a regular grid in latitude and longitude (with 0.5 degree spacing). The difference of the TBs of the 19 GHz V and H channels (dTB_{19}) was calculated for each grid point and then averaged over a year. If the mean annual difference of dTB_{19} was higher than 15 K the area corresponding to that grid point was identified as desert or arid land. ***Figure 06*** shows the results of this procedure. It is clear how the Sahara desert and the Arabian desert have been correctly identified as arid land. Smaller areas of arid land also appears in Iran (including the Dasht-e Kavir and the Dasht-e lut deserts) and in the African continent (including the Kalahari desert in South-West Africa and arid regions in the continental Horn of Africa). However some small deserts close to the coast have been not correctly identified, i.e. the Namib Desert in Namibia and the Danakil Desert in the African coast of the Red sea. The coast pixels have been excluded from this test to eliminate the polarization difference due to the sea surface emissivity.

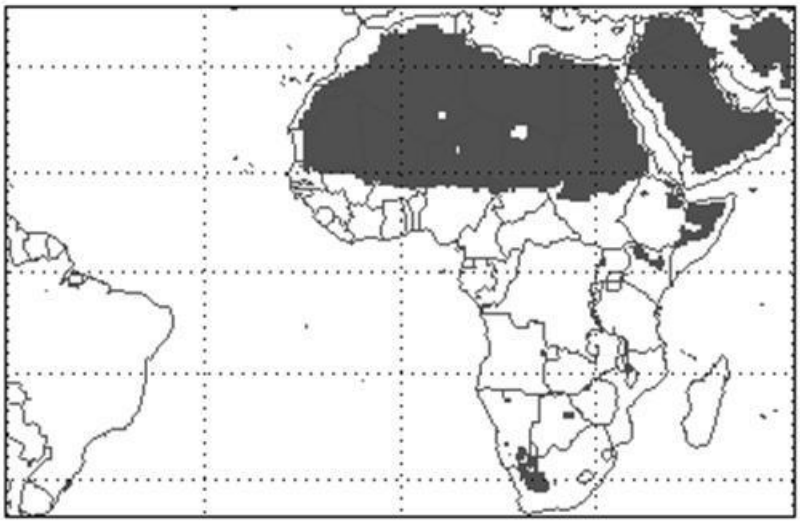

Fig. 06 - Map of areas identified as desert or arid land.

The screening for the Arid Land pixels is based on a Canonical Correlation Analysis (CCA) approach described in detail by Casella et al. (2015). The CCA approach marks as “rain” those pixels where:

$$CVs = \sum_{i=1}^{n} a_i (TB^i - \overline{TB}_m^i) > 2.4\ K$$

where the index *i* spans over the *n* available channels of the radiometer AMSU/MHS, TB^i are the brightness temperatures in each pixel, and $TB_m{}^i$ are the mean brightness temperatures for each channel computed over a full two year dataset (2011-2012) used in Casella et al. (2015) where the coefficients a_i, and the threshold value equal to 2.4 K have been derived. The coefficients of the CCA analysis (a_i) and the values for $TB_m{}^i$ are provided in **Table 03**.

Table 03: List of CCA coefficients and mean TB values used by the precipitation screening algorithm for Arid Land (desert)

AMSU A –MHS		Arid Land
Channel [GHz]	a	TB_m
89	0.07	231.00
157	-0.05	270.72
183.3±1	0.01	245.48
183.3±3	0.05	258.51
183.3±7	-0.08	267.58
23.8	-0.05	186.65
31.4	0.20	165.92
50.3	-0.29	230.79
52.8	0.13	261.44
53.6	-0.11	256.34
54.4	0.02	238.66
54.9	0.17	228.55
55.5	-0.08	215.23

3.3 The Precipitation Retrieval Algorithm

3.3.1 The neural network approach

As mentioned in section 2.1, the estimation by a physics-based direct inversion of the data would be difficult because of the changing viewing angle across a scan passage, and the concomitantly changing atmospheric path, introducing view angle-dependent errors in the RTE modelling system (RMS) calculations. When view-angle dependent errors enter retrievals, they complicate how systematic error should be expressed and impose a reduced confidence in formulating Bayesian probabilities. It is this confidence issue that motivates the use of neural network approach when using cross-track scanner data. We find that an ANN is able to overcome some of the view angle-dependent uncertainties. Moreover, as it will be explained later, the training database built for the retrieval for cross-track scanners is 45 times larger than the database used in the Bayesian CDRD approach because of all the viewing angles to be considered. In the ANN approach, the database is used only once during

the training phase. In a Bayesian approach the use of such a large database would significantly slow down the retrieval process.

The basic structure of the algorithm includes some signal processing components, as showed in previous sections, and a neural network as shown in ***Fig. 07***. The signal processing components process the data into forms that characterize the most important degrees of freedom related to precipitation rate such as atmospheric temperature profile, water vapour profile, cloud top altitude, particle size distribution, and vertical updraft velocity. The neural net is trained to learn the nonlinear dependencies of precipitation rate on these variables.

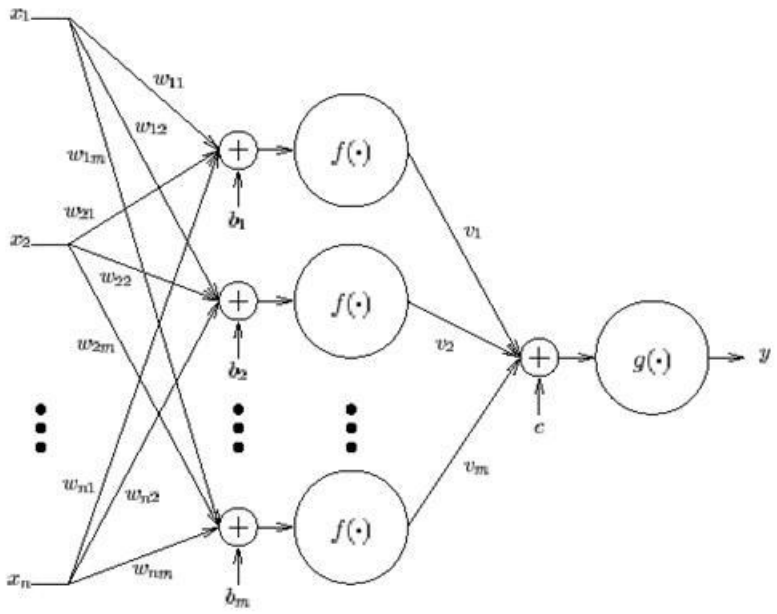

Fig. 07 - A 2-layer feedforward neural net with one output node.

The dependence of precipitation rate on these variables should be monotonic, so the neural net does not need to be complicated. A feedforward neural net with one hidden layer of tangent sigmoid nodes (with transfer function f(x) = tanh x) and one linear output node should be sufficient (Lippmann 1987).

The relative insensitivity of the ANN inputs to surface emissivity is important to the success of this technique over land, ice, and snow.

The statistical nature of precipitation must be adequately addressed during the training of the neural net. In addition to minimize the root-mean-square error between the estimated rain rate and the ground truth, one should also make sure that the estimator provides estimates that closely reflect the precipitation regime observed by the radiometer. Drizzle can have precipitation rates as low as 0.25 mm/h while tropical downpours can have rates as high as 200 mm/h (Ulaby et al. 1981). Precipitation rates can have a lognormal distribution with a standard deviation that is at least twice the mean (Kedern et al. 1994).

3.3.2 Training the ANN by CRM simulations

Since the relationship between precipitation and satellite brightness temperatures is nonlinear and imperfectly known, the retrievals here employ neural networks trained with tested physical models.

The training database used for the PNPR algorithm to deliver H SAF P-IN-MHS product is based on the same physical foundation used for the P-IN-SSMIS product for SSMIS (based on a physically-based Bayesian algorithm, using a Cloud Dynamic Radiation Database (CDRD), see Casella et al., 2013, and Sanò et al., 2013)) -- including the same cloud resolving simulations and RTE modelling methodology for calculating simulated satellite TB vectors consistent with the AMSU-A and MHS channel frequencies, viewing angles and view-angle dependent IFOV sizes along the scan projections. While the CDRD algorithm uses its database repeatedly to obtain *a priori* potential solution profiles for its Bayesian solver for retrieval situations at the times they occur, the PNPR algorithm uses its database only once during the training process, to develop the functional relationships needed between the inputs (*i.e.*, radiometer TBs, geographical/seasonal factors, pixel view angle) and the outputs (*i.e.*, surface precipitation rate, phase flag, and quality index).

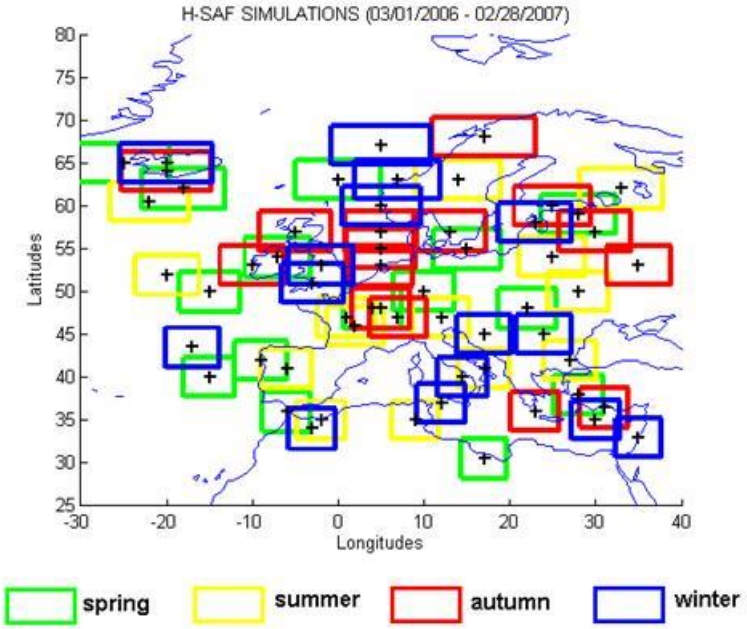

Fig. 08 - Inner domains of the 60 NMS simulations over the H SAF area, divided by season

The dataset for P-IN-MHS has been expanded to include simulations over Africa and Southern Atlantic. The original dataset used, for the H SAF area, was made of sixty simulations of different precipitation events over the European area for the period between March 2006 - February 2007 taking into account the various climatic regions, types of precipitation and seasonal variations. ***Fig. 08*** shows the inner domains of the 60 simulations. The database was made of 15 simulations for each season, selected in order to have the database as complete as possible.

For P-IN-MHS this dataset has been expanded to include 34 more simulations representative of the climatology and precipitation systems characteristic of Africa and Southern Atlantic (Panegrossi et al., 2014). The events have been selected on the basis of the Tropical Rainfall Measuring Mission (TRMM) Precipitation Radar (PR) observations (in particular the Rain Type flag and the Freezing level height) to select specific events over different climatic regions (shown in ***Fig. 09***) and to cover as much as possible the climatic variability in the area of interest with a limited number of simulations.

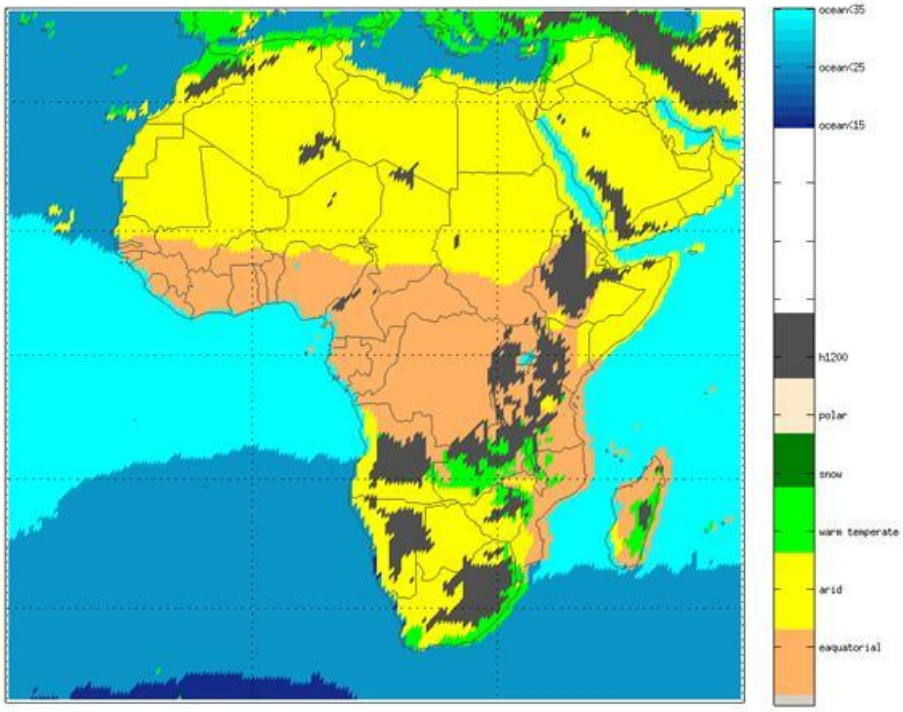

Fig. 09 – Climatic regions identified over the African continent and represented in the database used in P-IN-MHS

Figure 10 shows and example of a TRMM PR overpass over Africa, with PR derived rainfall rate, freezing level height and rain type for one of the simulated events occurred on 02/08/2007. **Table 04** provides the list of all cases selected to generate the database for the African regions, while ***Fig. 11*** shows the map of the spatial distribution of the inner domain of the 34 simulations over Africa.

All simulations have been carried out using the cloud resolving model University of Wisconsin-Non-hydrostatic Modeling System (UW-NMS) (Tripoli, 1992, Tripoli and Smith, 2014).

For each simulation, three two-way nested grids are configured. The vertical grid extends to 17 km divided into 36 levels with variable, height-dependent grid spacing. The horizontal grid configuration is comprised of: (1) an outer domain of 4,500 x 4,500 km at 50-km resolution, (2) a first interior domain of 900 x 900 km at 10-km resolution, and (3) a second interior and innermost domain of 500 x 500 km at 2-km resolution. Simulation cases are selected to ensure thorough sampling over an extensive manifold of multi-channel TBs and across a wide range of meteorological and microphysical conditions containing precipitation.

Each simulation was run for 24 or 36 hours for the European database, and 48 hours for the African database with a 12-hour spin-up time. This initial period is necessary to better initialize the model by adapting the initial data to the maximum resolution of the model. The NOAA National Center for Environmental Prediction (NCEP) Global Forecasting System (GFS) gridded analysis fields at about 100 km resolution were used as initial conditions and to nudge the boundaries of the outer grid every six hours throughout the simulation period. After the first 12 hours, the model extracts hydrometeor profiles over the inner domain 3 – this is done every hour of the remaining simulation time.

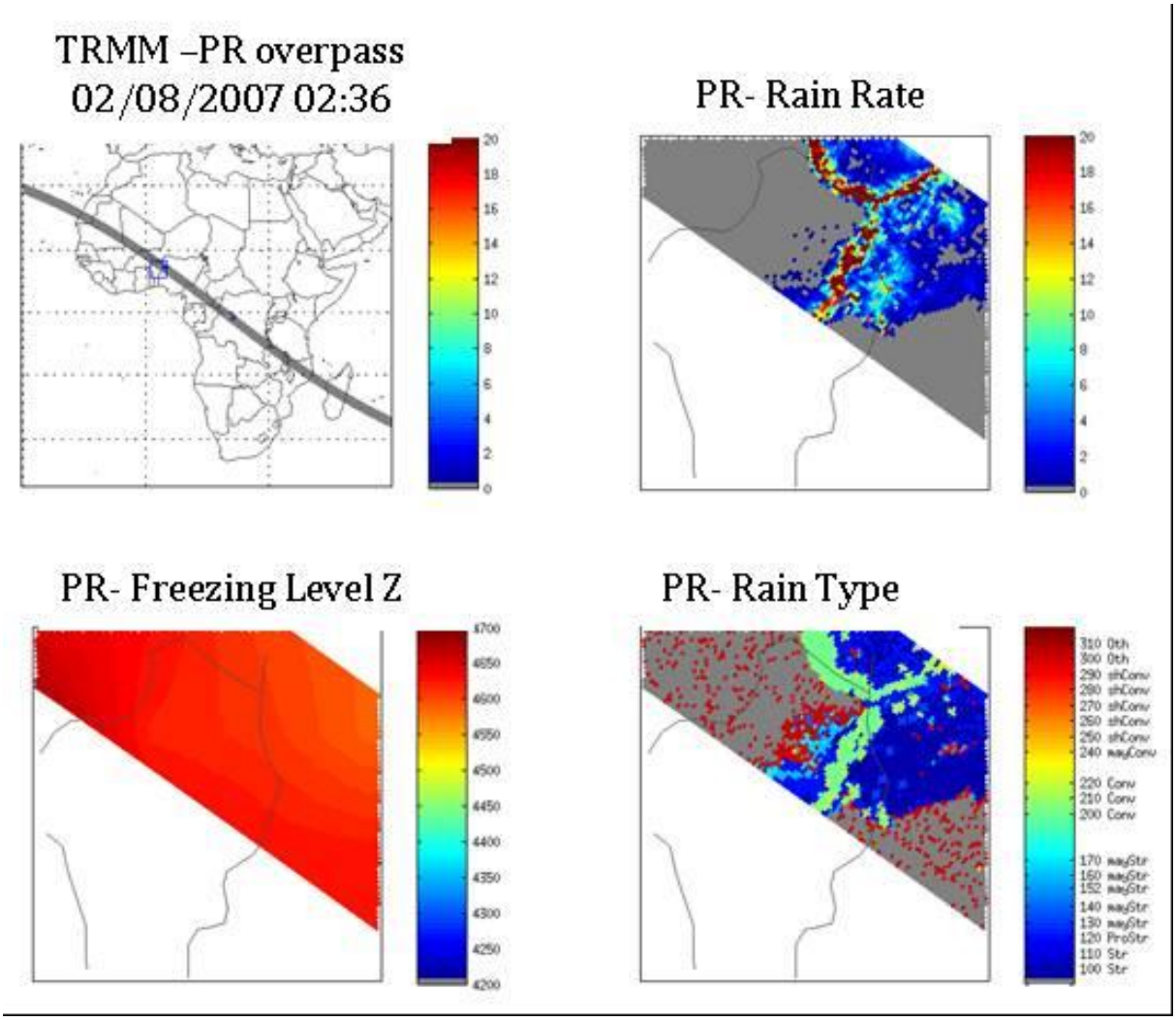

Fig. 10 **- Example of a TRMM PR overpass over Africa at 02:36 UTC on 02/07/2008 and detail of the area affected by the precipitation with PR derived Rainfall rate (mm/h), Freezing level height (m) and rain type**

Table 04: List of all simulations used to generate the African database for P-IN-MHS.

#	EventKind	ClimaticRegion	Date	UTC time	Lat.	Lon.	NOTE
1	A	1	20/02/2007	00:00	-25,00	42,00	TrCyFavio (madagascar)
2	A	12	21/08/2006	00:00	8,00	-15,00	tropical storm debby West Africa/Atlantic
3	A	4	23/07/2006	00:00	11,00	34,50	floods over Ethiopianhighlands
4	A	2	03/06/2010	17:16	22,00	59,00	TropicalCyclonephet (Oman)
5	B	1	17/07/2008	06:21	8,81	15,83	Storm over Nigeria-Ciad
6	B	2	18/06/2006	16:52	17,00	11,80	scatteredprecipitation Niger
7	B	1	02/08/2007	02:36	10,50	3,19	MCS Benin
8	B	1	20/09/2007	01:33	1,50	20,14	MCS NW Congo - fast growing

#	EventKind	ClimaticRegion	Date	UTC time	Lat.	Lon.	NOTE
9	B	2	03/10/2007	20:49	-21,44	26,52	NE Botswana storm after front
10	B	4	07/04/2007	14:30	-22,65	45,64	Madagascar (orographic)
11	B	1	09/10/2007	03:40	-1,00	25,00	MCS line CONGO
12	B	4	26/05/2006	23:26	32,50	-3,00	Storm over Atlas
13	B	2	29/01/2006	15:22	24,50	6,00	MCS Sahara Algeria
14	B	3	10/12/2006	04:01	-26,70	31,00	Storm Swaziland
15	B	12	11/04/2006	17:30	-3,70	0,70	MCS Guinea Gulf
16	B	1	19/03/2007	23:49	-3,50	14,00	MCS WestCentral
17	B	2	15/07/2006	19:41	14,00	-8,00	MCS Sahel
18	B	3	21/04/2007	01:13	32,50	-6,00	Storm front North Morocco
19	B	11	20/01/2006	17:02	32,80	-24,00	Storm North Atlantic Ocean
20	BCDE	12	14/10/2007	15:19	2,19	-11,63	Mixed Guinea Gulf
21	BD	1	13/05/2006	01:01	8,61	25,50	Stratiform-Convective Sud Sudan
22	BD	2	05/04/2006	20:04	22,94	48,33	Stratiform-ConvectiveSaudi Arabia
23	BD	2	05/02/2006	22:06	-26,11	22,19	Stratiform-Convective Botswana
24	BD	12	18/03/2007	01:41	-11,90	12,17	Stratiform-Convective Angola coast
25	CE	11	16/11/2007	04:20	-32,65	-25,08	Shallow-warm line South Atlantic
26	CE	1	06/08/2007	23:50	-16,25	49,99	Shallow-warm Madagascar
27	CE	2	29/01/2006	05:41	16,98	39,43	Shallow-warm Red Sea
28	CE	2	10/05/2007	03:27	-34,90	20,35	Shallow-warm line South Africa
29	D	2	16/02/2006	23:18	18,49	-5,36	Stratiform Sahara Mauritania
30	D	2	30/03/2007	13:35	31,52	21,85	StratiformLybia NE
31	D	6	16/12/2006	23:07	-12,70	25,96	Stratiform round Zambia
32	D	1	29/01/2007	00:20	-10,55	37,44	Stratiform Tanzania

#	EventKind	ClimaticRegion	Date	UTC time	Lat.	Lon.	NOTE
33	D	6	25/10/2006	22:09	8,65	43,62	StratiformEthiopianHighlands
34	D	12	22/09/2006	15:05	-2,10	59,49	Stratiform intense N-Indian Sea

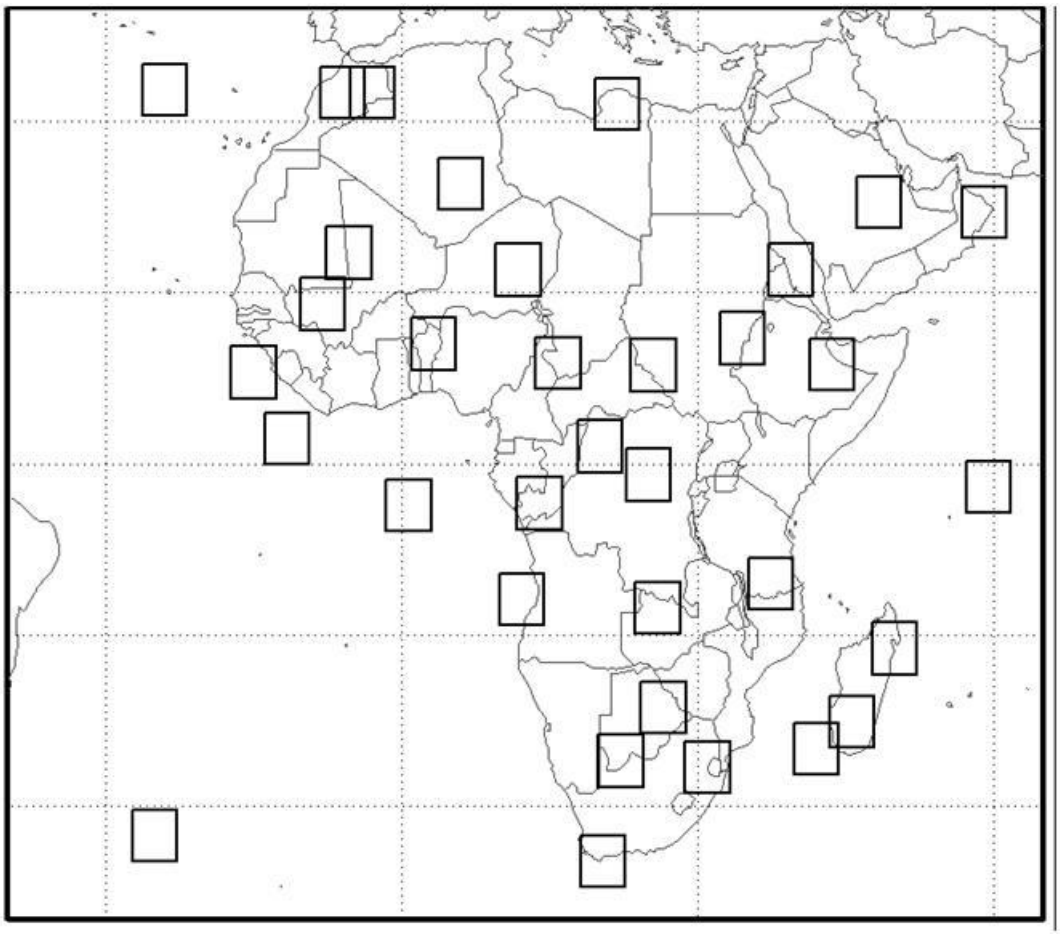

Fig. 11 –Spatial distribution of the Inner domain of the 34 NMS simulations over the African region for the P-IN-MHS training database

Each simulation used to build the training cloud-radiation database has been compared with available spaceborne observations (LEO-PMW, GEO-IR and TRMM-PR) to verify consistency of the simulated precipitation events with the observed scenario, and with the overall characteristics described in **Table 04**. Moreover, the simulated brightness temperature multidimensional manifolds have been subject to a detailed analysis aimed at verifying the representativeness of the database (see Casella et al., 2013).

3.3.3 The UW-NMS Cloud Resolving Model

The UW-NMS model represents the further development of the regional atmospheric modelling system (RAMS) maintained at Colorado State University (see Tripoli and Cotton 1981, 1982, 1986; Cotton et al. 1982, 1986; Tripoli 1992 a,b) with more recent major improvements concerning the model's dynamical conservation properties and its unique variable step topography (VST) surface coordinate system

described by Tripoli and Smith (2014). The NMS is a 3-dimensional, non-hydrostatic, nested, scalable regional-mesoscale, prognostic model. It is able to simulate atmospheric phenomena across all relevant scales from microscale, up through mesoscale and out to the synoptic/regional scales. This model is chosen because of its ability to achieve accuracy in simulating scale-interaction processes through imposition of conservation on mass, energy, momentum, vorticity and entropy throughout model integration. The underlying model framework uses quasi-compressible closure formulated on an Arakawa "C" grid cast on multiple-nest rotated spherical grids using multiple two-way nesting. The model employs non-Boussinesq dynamics, two-way grid nesting exchanges, and a unique terrain-following VST vertical coordinate system at its lower boundary. The two-way interactive nesting scheme allows increased resolution in focused areas. VST coordinates are able to capture the dynamical consequences of either steep inclinations or subtly varying terrain features without sacrificing accuracy for any type of terrain-induced slope flows at any scale as shown in Tripoli and Smith (2014). A variable ice-liquid water potential temperature is used as the predictive thermodynamic variable in the model (Tripoli and Cotton 1981). The advantage in using this quantity is its conserved properties for all phase changes. In so doing, potential temperature, water vapor and cloud water are all treated as diagnostic variables.

The UW-NMS microphysical module used for this study is a modified form of the scheme described by Flatau et al. 1989 and Cotton et al. 1986, and more recently improved by Panegrossi (2004). Specifically, in UW-NMS the treatment of ice categories and specifics of the precipitation physics tendencies has been modified from the original published works to enhance their performance. The microphysics is a bulk microphysics parameterization, which includes six hydrometeor categories labelled as: suspended cloud droplets, precipitating rain drops, suspended pristine ice crystals, and precipitating low-density graupel particles (or snow pellets), ice aggregates and high-density graupel particles. Depending on the application, all or some of these categories may be selected. Any combination of frozen and liquid hydrometeors can coexist within the same grid volume at any given time to allow hydrometeor category interaction to take place.

A negative exponential size distribution *N(D)* is assumed for all categories (except cloud droplets and pristine crystals, which are considered monodispersed), and it is given by:

$$N(D) = N_0 e^{-\lambda D}$$

Where N_0 is the intercept and λ is the slope of the distribution. The total concentration of hydrometeors in the distribution can be found by an integration of the distribution:

$$N_t = \int_0^\infty N(D)dD = N_0 / \lambda$$

The mean diameter and the liquid water content are quantities frequently used in cloud modelling applications. The mean diameter D_m is the first moment of the distribution, and it is defined as:

$$D_m = \frac{\int_0^\infty DN(D)dD}{\int_0^\infty N(D)dD}$$

For a negative exponential it becomes:

$$D_m = \frac{1}{\lambda}$$

The liquid water content or ice water content is proportional to the third moment of the distribution:

$$l_h = \int_0^\infty m(D)N(D)dD$$

Where *m(D)* is the mass of particles of diameter D. For spherical particles of density ρ_h with negative-exponential size distribution, it becomes:

$$l_h = \pi N_t D^3 m \rho_h$$

An alternative to the liquid water content to describe the mass content of hydrometeors within the cloud is the mixing ratio defined as:

$$r_h = \frac{l_h}{\rho_0}$$

where ρ_0 is the dry air density. It is always predicted in UW-NMS, and it is related to the size distribution parameters by:

$$\lambda = \left[\frac{\pi \rho_h N_t}{\rho_0 r_h} \right]^{\frac{1}{3}}$$

One can see that the distribution can be completely described by assigning a value of either the slope, or the intercept, or the concentration. The model always predicts the total mixing ratio of all condensate (liquid and ice), water vapor mixing ratio, and the mixing ratio of each hydrometeor category, except for cloud droplets whose mixing ratio is diagnosed.

For each hydrometeor category, the UW-NMS model offers the possibility to specify the value either for the slope, or for the intercept, or for the total number concentration. A different method for parameterising each hydrometeor category can be selected where the total concentration (number of particles per unit mass) can be predicted. This option allows the parameters of the size distribution λ and N_0 to be diagnosed from the mixing ratio and the total concentration, obtaining different values of the slope and the intercept at each grid volume. Mixed-phase particles (i.e. melting graupel) are not included but any combination of liquid and frozen particles is allowed to occur at a given grid point.

For the aim of this project it is very important to describe the parameterization of each hydrometeor category, explaining the major assumptions in the conversion process between one category and the other, and to describe the parameterization of their microphysical properties. Particular emphasis will be given below to the size distribution and density (for the frozen hydrometeors) parameterization, because these are the parameters that directly determine the optical properties

A - Cloud droplets **-** The cloud water drops are assumed to be of constant size except with respect to the formulations for autoconversion and ice splintering where they are cast in the form of a modified Gamma distribution (Tripoli and Cotton 1981). Their mixing ratio is diagnosed, while their concentration is specified *a priori* since cloud water nucleation is not explicitly considered in the model. The typical characteristic diameter (D_C) of cloud droplets is 0.02 mm with the density of pure water (ρ_w), *i.e.*, 1 g cm^{-2}. Besides the implicit diffusional growth and decay of cloud water due to production of supersaturation built into a diagnostic system, cloud water may be converted to any of the other hydrometeor categories through collection, phoretic contact freezing, or autoconversion directly to rain. Stochastic broadening is parameterized to be dependent on the average cloud-droplet size.

B - Rain drops – For this study, the rain water category is assumed to be distributed in a Marshall-Palmer distribution of specified constant intercept of 0.08 cm^{-4}. Rain droplets arise primarily through the collision-coalescence process (warm rain) and the melting of precipitating ice particles (cold rain). In warm-based clouds, like those typical of summertime Alabama or tropical cyclone, both processes are important. Rain droplets are lost to the system primarily through conversion to ice categories (droplet freezing and riming) or evaporation and through loss due to precipitation.

C - Pristine ice crystals - The original pristine ice category of the Flatau parameterization (Flatau et al. 1989) is divided into a snow and pristine category. The original version grouped both nucleated and new crystals together. Since a constant size distribution had been assumed, massive nucleation at cold temperatures would drastically alter the average crystal size and would remove all memory of the growth that some of the larger crystals had been through. Here, riming growth processes are assumed to convert pristine crystals at their predicted mass to a snow category which represents rimed crystals. Hence, new and mature populations of crystals continue to exist as pristine crystals where massive nucleation occurs, whereas crystals that have substantially increased in mass through riming are separated out in can evolve independently. This was especially important for the simulations of cirrus anvils where influxes of pristine crystals would dominate the old inclusive pristine category sometimes preventing the precipitation of the rimed particles .Both their concentration and mixing ratio are predicted, therefore their mass and size change at each grid point, with a typical D_C of ~0.24 mm. The density (ρ_p) is derived according to Flatau et al. (1989), starting with a mass - diameter (m - D) relationship:

$$D = \beta\left(\frac{m}{K}\right)^{\alpha}$$

Where α is a non-dimensional exponential factor,β is a size scale factor (in cm) and K is a mass normalization factor (in g). For an equivalent volume sphere, the density becomes:

$$\rho_p = \frac{6}{\pi} K \beta^{\alpha} D^{1/\alpha - 3}$$

The three parameters, α *(=0.5)*, β (=19.2 cm) and *K (=1g)* depend on the crystal mass in such a manner that as the mass (or size) increases, the density decreases (see Casella et al., 2013 and Smith et al., 2013 for further details). The only source of new crystals are primary and secondary nucleation including sorption and deposition, contact nucleation and splintering. Pristine crystals can be lost through conversion to hard graupel resulting from collection directly onto the graupel surface or through contact freezing of rain droplets, by conversion to soft graupel through the riming of cloud droplets or the conversion to aggregates through the aggregation process. Because pristine ice crystals tend to remain quite small in mass, they can be assumed to melt instantaneously when the temperature of the air exceeds freezing.

D - Ice aggregates / Snowflakes - The aggregate category consists of aggregated crystals formed by collisions among pristine crystals, or pristine crystals other aggregates. Aggregates are assumed to be in a Marshall-Palmer distribution of constant assumed slope, with mean radius of 1650 μm. The implicit assumption is that break-up balances formation. Additional growth is possible from riming and deposition, although strong riming will result in conversion to graupel at a specified rate. Aggregates represent the major source of graupel embryos. Aggregates are lost to melting, evaporation, precipitation fallout processes and conversion to snow pellets through riming processes. For aggregates the size dependent density $\rho_{s/a}$ is given the above equations, where α = 0.419 and β = 8.89 cm. The resultant expression is $\rho_a\ (D_C)$= 0.015 / [$D_C^{0.6}$] g cm^{-3} (Panegrossi et al., 1998)

E - Soft graupel / Snow pellets - The snow pellets (or soft graupel) category is assumed to follow a Marshall-Palmer distribution with constant intercept of 0.014 cm^{-4}. The snow pellets are assumed to grow

from their initiation size through vapor-deposition processes and riming of both rain and cloud droplets. There is an assumed conversion formula to convert the soft graupel to the hard graupel category, which is dependent on the riming rate by rain droplets compared to growth rates by other processes and the relative size of collected rain droplets compared to the snow particle size.

Snow represents soft, low-density ice forming when pristine crystals or aggregates become heavily rimed, with their density (ρ_s) formulated according to Macklin (1962):

$$\rho_s = \left(-\frac{\hat{r}\hat{U}_{imp}}{T_s} \right)^b$$

in which T_S is the surface temperature of the ice substrates (in ℃), $\hat{r}$ is a weighted averaged radius (in μm) and $\hat{U}_{imp}$ is the weighted average impact velocity of cloud droplets and rain drops (in $m\ s^{-1}$). The values for the *a* and *b* coefficients are 0.23 g cm^{-3} and 0.44, respectively, as reported by Prodi *et al.* (1991). The $\hat{r}$ is calculated by averaging the radii of the cloud droplet and rain drop diameters, weighted by their respective mixing ratios. The $\hat{U}_{imp}$ is calculated by averaging the impact velocity between rain drops and snow (*i.e.*, the difference between the terminal velocities of rain drops and snow) with the impact velocity between cloud droplets and snow (*i.e.*, approximately the terminal velocity of snow alone), again weighted by the mixing ratios of cloud droplets and rain drops. The resultant snow density typically covers a range of values from 0.05 - 0.9 g cm^{-3}.

F - Hard graupel / Hailstones - The hard graupel category is also assumed to be in a constant intercept (0.071 cm^{-4}) Marshall-Palmer distribution and constant density ρ = 0.9 g/cm^3. Hard graupel grows or decays from vapour deposition, riming, and melting and conversion from rain, pristine crystals, aggregates and soft graupel categories. Wet growth or dry growth are both modeled and depend on the diagnosed equilibrium temperature of the graupel surface. This temperature depends of the energy balance at the surface of the droplet resulting from conduction with the air versus latent heating or cooling due to evaporation or sublimation onto the particle, and freezing of collected liquid water. At sub-freezing, air temperatures, the energy balance determines the proportion of any collected liquid water that can be frozen, given the rate that the particle can conduct heat away to the air. Any excess water that cannot freeze is assumed to be shed as rain. Hence wet or dry growth or melting is modeled at below or above freezing temperatures dependent on the diagnosed energy balance. The results of this balance can be made available for radiative transfer calculations since the existence of a liquid coating dramatically alters radiative properties of the graupel particle.

3.3.4 The Radiative Transfer Model

AMSU-A and MHS radiances were simulated by using a one-dimensional plane-parallel Eddington approximation to the inelastic, steady-state RTE (see Liou, 2002]). The plane-parallel Eddington approximation is well known and widely used especially because of its computational efficiency. It is important to recognize that for the most part, the mean PMW TB differences between a one-dimensional RTE model and fully three-dimensional RTE model (either through use of an analytical approximation scheme or a generalized Monte Carlo method) are within a few degrees in magnitude (see Roberti et al., 1994, Smith et al, 2002) even considering the use of the higher SSMIS frequencies (see Bauer et al., 2006). Although these differences may become significant locally in case of strong horizontal gradients within the cloud microphysical properties such as near cloud edges (*e.g.*, Liu et al., 1996), we have found in our own calculations that the treatment of the optical properties of the ambient hydrometeors and their concomitant treatment in a single scatter framework is far more

important in reconciling RTE model calculations with satellite observations, than the particular choice of the core RTE model solution. The last argument is in accordance with the recent study of Kulie et al. (2010) based on several ice scattering models compared within the framework of both passive and active microwave models.

Namely, every vertical profile generated by the model at high resolution is used to generate a plane-parallel precipitating environment, to which the RTM is then applied to compute the upwelling TBs at the different incident viewing angles of the radiometers. The required inputs to the RTM are: suitable temperature/moisture profiles and temperature/emissivity of the surface, as well as vertical profiles of liquid/ice water contents (LWC/IWC) of the various hydrometeors - along with their single-scattering properties. Surface temperature and vertical profiles are provided by the UW-NMS simulation. Absorption by atmospheric gases at microwave frequencies are calculated according to the Liebe and Gimmestad (1978) and Liebe (1985) clear-moist air refractivity model that provides a combined water vapour – oxygen volume absorption coefficient.

The same 9-member surface emissivity module (SEM) developed and used for the CDRD (P-IN-SSMIS) algorithm has been used to generate the training database for P-IN-MHS. For a rough ocean (*i.e.*, an ocean surface undergoing above-surface winds) the SEM employs the ocean emissivity model of English and Hewison (1998); see also Schluessel and Luthardt (1991) and Hewison and English (2000).

This scheme calculates accurate estimates of open sea emissivity between 10 and 200 GHz for observation angles up to 60 degree sand winds between 0 and 20 m s^{-1}. For non-frozen land emissivity, we have adopted two different surface emissivity models from Hewison (2001), specifically models for “other forestry” and “bare soil”, which we refer to as “vegetated land cover” and “non-frozen bare soil”, respectively. For frozen surfaces we have adopted six surface emissivity models from Hewison and English (1999) consisting of “frozen bare soil”, “snow-covered forest”, “first year ice”, “compact snow”, “fresh wet snow”, and “deep dry snow” -- noting we have imposed various minor name changes from the originals for the frozen surface cases. We also note that the latter four frozen surfaces may be applied to either ocean or land areas. For desert areas (arid land) the model uses the TELSEM emissivity atlas (see Prigent et al., 2006).

For calculations of the single scattering properties of hydrometeors, various assumptions concerning hydrometeor shape are made, since shape information is not comprehensively provided from the NMS bulk microphysical parameterization scheme. In NMS, cloud droplets and raindrops are considered to be spherical and homogeneous, thus their scattering properties can be calculated based on Mie theory. Graupel hydrometeors are assumed to be spherical and homogeneous with a bulk density (mass /volume of a circumscribing sphere) equal to ρ_g (0.9 g/cm^3). Thus Mie theory can also be used to calculate graupel optical properties using the index of refraction of a homogeneous mixture of air and ice, according to the average dielectric function of Maxwell-Garnett.

In NMS, pristine crystals represent recently formed particles and are assumed to have a hexagonal plate habit, and size/density formulations described in Section 2.1. Alternatively, the RMS represents pristine crystals as many different simple ice crystal shapes, from needles to plates, all assumed to have the same D_C of 0.024 cm which results in an associated density of 0.1 g cm^{-3}. In order to calculate their optical properties, the Grenfell and Warren (1999) approximation scheme is used. In this approximation, the single-scattering properties of each non-spherical particle are calculated by means of a collection (concentration) of solid ice spheres n_S, all equal in size to one another, with a new equivalent diameter (D_S) determined by the ratio of volume over cross-section area (V / A_{cs}) of the original particle. The V factor is derived from the NMS. To obtain the A_{cs} factor, the following relationship is used:

$$A_{cs} / (\pi D_c^2/4) = K_0 D_c^k$$

for various shapes of ice particles. For our calculations, K_0 and k are taken as 0.18 cm^{-1}and 0.2707, respectively, as indicated by the aforementioned authors for continental cirrus with mixed habit (noting the circumscribing sphere characteristic diameter D_C must be expressed in cm). The result is that the D_S and n_S of the equivalent spheres is given by:

$$D_s = \frac{\rho_p}{\rho_i}\frac{D_c}{K_0 D_c^{\,k}}$$

$$n_s = \left(\frac{K_0}{1-k}\right)\left(\frac{D_c^{3+k}}{K_0 D_s^3}\right)$$

In the NMS, snow and aggregates are porous, low-density and assumed to have variable complex shapes. In order to represent snow and aggregates as non-spherical particles, we adopt the approximations developed by Surussavadee (2006), Surussavadee and Staelin (2006, 2008a,b) in which the results of several single scattering simulations of non-spherical particles have been reproduced synthetically using the Mie solution for spheres of equivalent mass and a density formulation ρ(ν) that is a function of frequency (ν). In this fashion, both radii and densities of the simulated hydrometeors are changed to take into account the optical effect of non-sphericity, without altering their masses. In detail, snow and aggregates are approximated by equal-mass spheres that are mixtures of ice and air having densities 0 < $\rho(\nu)$ < 0.9 g cm-3 that depend on habit and ν. It is important to note that $\rho(\nu)$ is that of an optically-equivalent particle and can be quite different from the density of hard ice, as well as different from the bulk density of the original particle itself. The formulation is:

$$\rho(\nu) = \gamma \cdot 10^{-3} \cdot \nu + \eta$$

where for snow (corresponding to plates), the parameters γ and η are 0.815 g cm^{-3} s^{-1} and 0.012 g cm^{-3}, respectively, while for aggregates (corresponding to 6-arm bullet rosettes) they are 0.863 g cm^{-3} s^{-1} and 0.115 g cm^{-3}, respectively and ν is expressed in GHz.

Once individual absorption, scattering, and asymmetry factors have been calculated for the components hydrometeors of a vertical grid cell, they are integrated over the PSDs to obtain bulk absorption / scattering efficiencies and asymmetry factors for the entire microphysical mixture. This process then continues throughout the vertical extent of the microphysical profile. Next, the boundary emissivity (reflectance) from the surface is obtained from the SEM (see next sub-section). Finally, the multiple scattering RTE model is invoked to obtain the simulated top of atmosphere (TOA) satellite TBs. Because Mie equations are used in calculating the scattering phase functions of equivalent spheres, the RMS's RTE model cannot introduce polarization to the radiation field due to the cloud hydrometeors themselves. However, polarization is introduced through the polarized reflecting surface backgrounds.

3.3.5 The Instrument model

The variability in precipitation cover within a given IFOV produces errors in retrievals because of the underlying non-linear relationship between TBs and precipitation rates, an effect referred to as non-uniform beam filling (NUBF) error. This is a critical issue for lower frequency/larger IFOV footprints and/or IFOVs situated at scan edges. To reduce NUBF errors, the initial simulated TBs for the database, initially taken at the CRM's 2-km resolution, are spatially averaged (convolved) using the AMSU-A/MHS Gaussian antenna pattern functions out to ±1σ widths, these functions varying with channel frequency and view angle. In replicating the characteristics of the AMSU-A and MHS radiometers, the RMS makes calculations at 45 beam centers (ϑs) using steps of 1.1°, equivalent to the number of mechanical scan

stops used on the MHS instrument, scanning to either side of nadir over a tilt angle from nadir beam center to edge beam center of 48.33° for a ½ scan angular view field of 49.5°. Therefore, each possible NMS cloud structure must be associated to 45 different TB vectors (for each of the 45 view angles), noting a complete MHS instrument scan involves 91 steps, but with angular symmetry around the center step. [Note the AMSU-A instrument uses a 3.3° angular step at 15 beam centers from nadir to either scan edge, again for a ½ scan angular view field of 49.5°.] The inherent problem of beam filling due to the low spatial resolution of the MW radiometers (in particular at the edge of the AMSU/MHS scan) contributes to the uncertainty in the retrieval and underestimation of the precipitation for convective and small scale events. To partially account for this problem, the quality index associated to the surface precipitation estimate accounts for the degrading quality of the retrieval as the scanning angle increases (see Section 3.3.8).

In the P-IN-MHS database, the correspondence between TB vectors, along with their associated surface precipitation rates, is complicated by the dependence of spatial resolution along a radiometer scan due to the varying view angle. A variable sensor resolution (VSR) is defined according to the nominal nadir resolution of MHS, varying from 16 x 16 km^2/circular at nadir to 26 x 52 km^2/ovate at scan edge. Thus, the surface precipitation rates must be averaged for 45 VSRs with precipitation products delivered to the H SAF product data center tagged accordingly. This means that the PNPR database is 45 times greater density in precipitation structure entries than the CDRD database, which itself contains some 2.5 million entries for the European / Mediterranean basin region.

3.3.6 The neural network

Like the human brain, ANNs are repeatedly exposed to inputs, responding by varying the strength of the connections between its neurons based on the inputs (see Haykin, 1998, 2009). Thus, learning for ANNs is accomplished by use of an iterative process, similar to say, relaxation-based inversion but unlike single step-based schemes such as use of regression equations or accumulations according to Bayesian probabilities. By the same token, a simplifying feature of the PNPR algorithm is that it uses a unique ANN that retrieves the surface precipitation rate for all types of surface backgrounds represented in its database, *i.e.*, land, ocean, ice, snow or coast. This approach prevents different precipitation estimates being inconsistent with one another when an observed precipitation system extends over two or more types of surfaces. Note the PNPR outputs consist of both the surface precipitation rate and a phase flag indicating liquid, frozen, mixed or unknown conditions. The PNPR algorithm cannot provide the liquid-total ratio for the mixed phase case, because unlike the CDRD algorithm, it does not retrieve vertical hydrometeor profiles for the six microphysical species.

As input data, the PNPR algorithm incorporates TBs measured by the AMSU-A and MHS radiometers. Beside the TBs (see **Table 05**) the algorithm uses various additional channel-derived variables.

Table 05: Channels utilized by the PNPR algorithm

Radiometer	TB (GHz)
AMSU-A	50.3±50
AMSU-A	52.8±105
AMSU-A	53.596±115
MHS	89±0.9
MHS	157±0.9
MHS	183.31±1
MHS	183.31±3
MHS	183.31±7

In order to reduce ambiguity, other geophysical inputs (*i.e.*, latitude, terrain height, surface type, season) guide the algorithm towards selecting database members that are most representative of an observed scene. The pixel number along the scan is an additional principal input parameter, needed to determine the degree to which limb smearing is to be reduced, an effect produced by the changing atmospheric path length along the scan (see Goldberg et al., 2001). The ANN itself performs this limb correction.

The procedure to design and test the NN is based on two criteria. The first criterion concerns the division of the training database into two pieces: the *ground truth (training)* piece to be used for the actual training, the *validation* piece for providing the synthetic TBs used in a subsequent verification analysis. Is often useful to create a third database (the *test database*) for providing the TBs for the comparison of the different NN's. Notably, all three pieces need to be representative of all precipitation events contained within the collective database. The choice of the size and of the specific members of each piece is thus crucial in obtaining an effective evaluation of the final NN's performance. Consequently, a statistical analysis was performed on each piece to check their representativeness of the different typologies of simulated events, and of the whole range of precipitation rates. The second criterion concerns the early stopping method, i.e. the interruption of the training before complete convergence has occurred in order to avoid the loss in generalization ability of the network. Through various experimental tests the early stopping method was refined in order to improve the generalization ability of the NN, in view of the size (several millions of profiles) and complexity (wide range of the precipitation values and different viewing angles) of the *training* database. In particular, we have found some optimal conditions for the gradient of the performance function of the NN [the performance function is represented by the mean squared error (mse)] and for the number of iterations (epochs) during the training. In fact, these two parameters provide an indication on the quality of the learning process of the network. The number of epochs was limited in the range 500-1000, and the minimum value of the gradient of performance (mse) was fixed to 0.05. The correlation coefficient (R) evaluated in the *training* dataset was limited to 0.90 while the corresponding minimum value in the *validation* dataset was set at 0.80. These values correspond to a balance between an appropriate learning level and a good generalization ability of the NN.

The design of the network architecture is normally determined empirically. Model selection in neural networks aims at finding as few hidden units and connections as necessary to have a good approximation of the true function. This selection includes two relatively distinct aspects: determining how many layers to use and determining how many nodes to include in each layer. Unfortunately, this is not a simple problem and turning to an empirical approach is often the most reasonable way. In this study the model selection has been carried out using a cross validation method (Anders and Korn, 1999; Marzban, 2009). The cross validation strategy is based on the mean square prediction errors (MSPE) which is obtained applying the ANN to different test datasets (obtained dividing the validation dataset into M subsets containing n observations each). The model is repeatedly re-estimated using different datasets of n(M-1) observations, leaving out a different subset each time. The average MSPE defines the cross validation error, CV (Anders and Korn, 1999):

$$CV = \frac{1}{M}\sum_{m=1}^{M} MSPE_m$$

Table 06 shows the ANN resulting optimal performance (R, MSE, CV) considering the training and the validation phase for different background surfaces.

Table 06: ANN synthetic performances for different background surfaces

LAND				OCEAN				COAST			
Training Database		Validation Database		Training Database		Validation Database		Training Database		Validation Database	
MSE	R	CV	R	MSE	R	CV	R	MSE	R	CV	R
0.32	0.91	**0.34**	**0.89**	0.30	0.93	**0.32**	**0.90**	0.42	0.89	**0.45**	**0.87**

In the cross validation methodology, the first step consists in determining the number of hidden layers. Starting from a simple architecture, two models are compared, one of which contains an additional hidden unit. For both the models the *CV* is evaluated and, if the more complex unit shows a smaller *CV* error, the additional hidden layer is accepted. The procedure stops when no further hidden layer is able to reduce the *CV* error. At this point, with a similar procedure, the number of nodes is optimized in each layer. The second step aims at determining the input connections. To find irrelevant connection, one input is removed and the resultant *CV* is compared with that of the complete network. In this way all the models with one input connection removed are analysed and the model with the lowest *CV* error is accepted. At the end of this second step, no input connection can be removed without increasing the *CV* error. Considering that there is a trade-off between the two steps, because the number of layers and the numbers of nodes in each layer are inter-dependent, the design tactic requires to alternately tune the number of layers, the number of nodes and the number of inputs.

During the phase of network design and the training process, more than 200 architectures have been tested and an optimal neural network has been obtained, where "optimal" refers to the best performance of the network (i.e., minimum *CV* over the full dynamic range of the inputs, absence of overfitting (i.e., the loss in generalization ability of the network), and absence of anomalous inhomogeneities in the retrievals).

The result of the training process is a three-layer ANN. In the 1st layer, the number of perceptrons (nodes) equals the number of TB + TB-derived inputs. For the 2nd and 3rd layers, twenty and eight perceptrons are selected, respectively. The use of the additional layers is necessary to prevent: (1) overfitting, measured by small values of *MSE* during the learning procedure followed by large values during the verification analysis, and (2) too little variability in precipitation rates along with an inability to identify consistently heavy precipitation. Once the optimal ANN is created, a final check of the retrievals is conducted to determine their stability as the input data vary. To accomplish this, the input TBs are perturbed with random noise within the allowed radiometric errors, followed by associated retrieval calculations. The perturbation retrievals are then compared to those obtained from the original TBs to obtain corresponding differences. Since these comparisons do not reveal significant differences, the stability of the optimal ANN is confirmed, enabling its effective implementation within the PNPR algorithm.

Figure 12 shows a flow diagram of the PNPR algorithm. First, the input TBs undergo a quality check to replace occasionally corrupted TBs with synthetic values created by the ANN using neighboring TBs at the same and different channel frequencies. Additionally, two maps of geographical and seasonal information are created for the observed scene. Then, four different procedures are carried out: (1) screening tests for detection of surface precipitation areas, (2) identification of areas where the algorithm is known to be less accurate, (3) creation of a map of initial quality indices based on procedure 2 and to be associated with the final surface precipitation retrievals, and (4) creation of an initial placeholder map of the phase flag of the final precipitation retrievals. Now the optimal ANN itself is applied, generating the final retrieved values of surface precipitation rate and associated phase flag. A separate element of the ANN controls the TB inputs for assigning the phase flag (see next section). To finish the retrieval process, the quality index is updated, taking into account the

magnitudes of the retrieved surface precipitation rates themselves, and sensor viewing geometry. Thus, besides the surface precipitation rate and its phase flag, the quality index for each retrieved pixel is also provided.

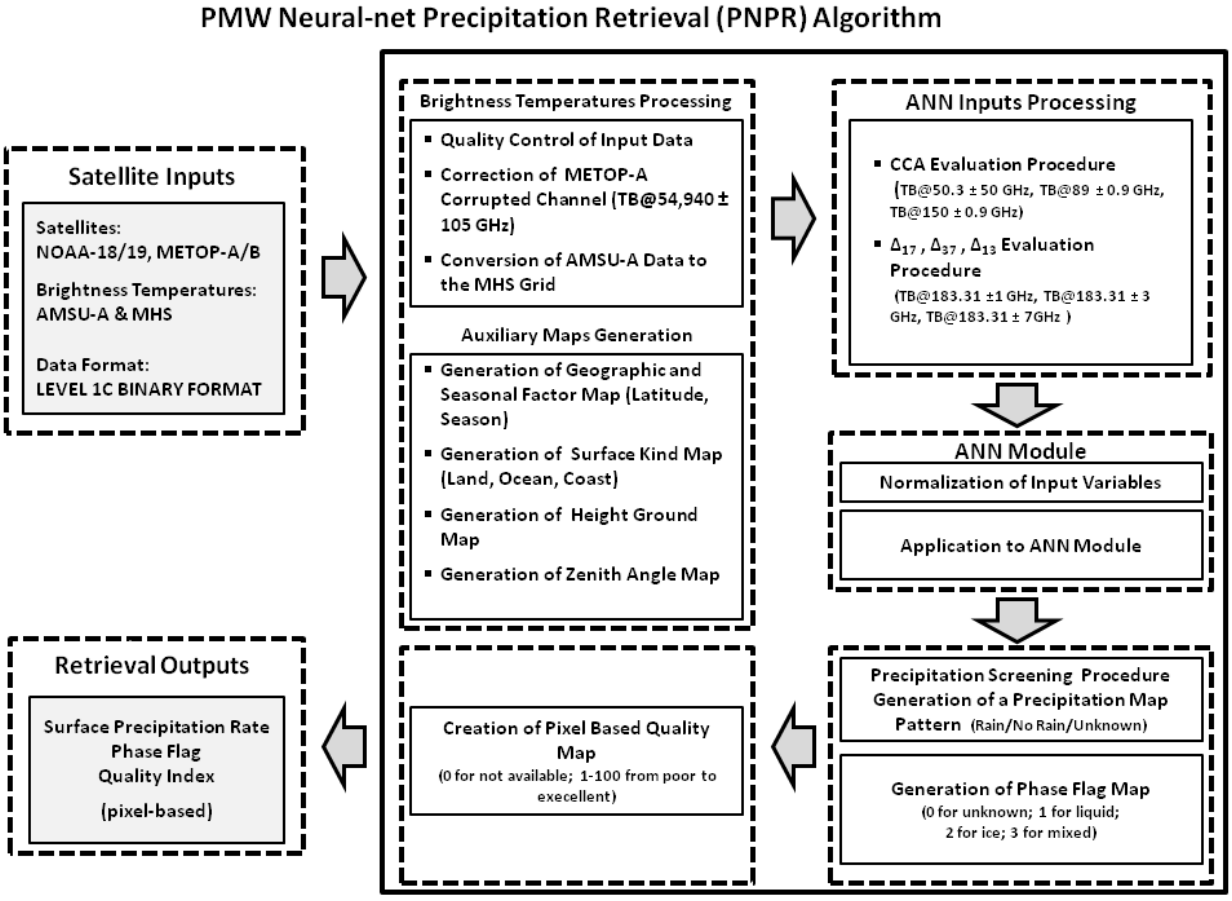

Fig. 12 - Flow diagram of the P-IN-MHS algorithm

3.3.7 Assumptions and limitations

Assumptions:

The design of P-IN-MHS product has been based on the use of a single ANN for different surface backgrounds. This approach prevents different precipitation estimates being inconsistent with one another when an observed precipitation system extends over two or more types of surfaces.

Furthermore the research has been focused on the design of one ANN able to take into account the limb effect and the changes of the spatial resolution along the scan.

Limitations:

Most of the limitations come from the radiometers resolution degrading with the scan angle and the related beam filling effects. The inherent problem of beam filling due to the low spatial resolution AMSU/MHS contributes to the uncertainty in the retrieval and underestimation of the precipitation for

convective and small scale events. Moreover the low frequency channels, which provide useful information over the ocean cannot be used effectively because of their low resolution.
To take account of these limitations, a pixel based quality index has been defined (see Section 3.3.8).

3.3.8 Quality Index and phase flag

In the last step of the P-IN-MHS product generation chain, a pixel based quality flag and a pixel based phase flag is computed.

Phase of precipitation
P-IN-MHS provides a phase flag associated to the surface precipitation estimates. The phase flag is based on the studies on snow and ice detection of Surussavadee and Staelin (2009) and Rosencrantz (2003). In these studies snowfall is detected by the use of TBs at 20.3 GHz, 50.3 GHz and 89 GHz , and on combinations of these TBs. The phase identification procedure compares the selected TB's and their derived quantity with some thresholds to distinguish between liquid or iced precipitation, and to be able to detect falling snow over snowy or iced background. The thresholds are based on the use of AMSU-A and MHS/MHS channels, and these same thresholds are used for P-IN-SSMIS and P-IN-MHS for H-SAF Area.

With reference to Grody et al. (2000), the following index are used to identify the presence of snow and ice background:

TT	=	$168+0.49\ TB_{89}$	(over land)
Scattering index (SI)	=	$TB_{23}-TB_{89}$	(over land)
DF	=	$2.85+0.020\ TB_{23}-0.028\ TB_{50}$	(over ocean)

Particularly, the snow/ice detection procedure (over land) is based on the relations (Grody et al. 2000, Rosenkranz 2003):

SI < 3 K and TB_{23} < 220 K (ice);
SI ≥ 3 K (snow);
DF > 0 and latitude > 50° (sea ice);
TB_{23} ≥ TT or TB_{23} ≥ 262 K (snow/ice cover, critical environmental conditions);

In the first tree cases the phase is solid while in the last case the phase is unknown due to the uncertainties in the screening of precipitation over ice/snow surface background in these conditions. Mixed phase is associated to pixels in the transition area between liquid and solid.
It should be noted that the detection and retrieval of solid precipitation consists of two steps. First, the ANN retrieves the value of the precipitation rate (either solid or liquid since the training database consists of both liquid and solid precipitation realizations). Then, the phase identification procedure allows to discriminate between solid and liquid precipitation.
The phase flag is evaluated only for pixels flagged as precipitating after the screening procedure and it is not available over coastal background surfaces.
The phase flag is given as an integer number according to **Table 07** of the standard output field associated. The integers will be associated as follows:

Table 07: Phase flag values and interpretation

Phase flag	Integer value
unknown (flag determination not reliable/no rain)	0

Liquid	1
Solid	2
Mixed	3
missing value (bad data, or precipitation retrieval not available)	7

Figure 13 shows an example of phase flag for a case study over Italy (10/02/2012).

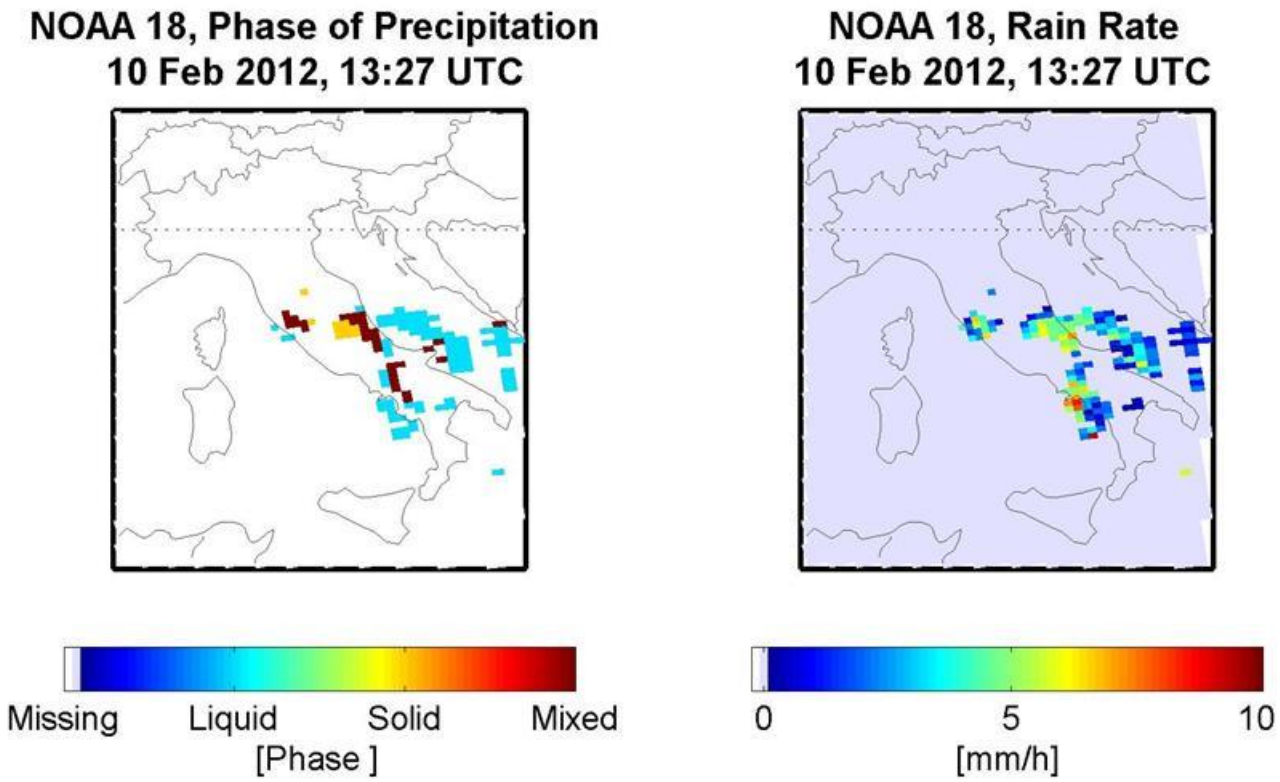

Figure 13: Example of phase flag for a case study over Italy. Left: Phase of precipitation; right: retrieved precipitation [mm/h]; NOAA 18 – 10 February 2012 13:27 UTC

3.3.9 The quality index

P-IN-MHS provides a quality index to be associated to the estimated value of surface precipitation rate. The quality flag summarizes the product quality and reliability and provides the end-users with a simple and immediate criterion for the evaluation of the products towards a correct selection and application of the precipitation estimates with respect to the analyzed scenario.
The quality flag (poor, fair, good, or missing, **Table 08**) is based on a Percentage Confidence Index (PCI) describing both the product quality and reliability, based on four different criteria:

1) ***Quality of input data*** (used sensor, type and number of channels used, horizontal resolution, malfunctioning of radiometers);
2) ***Background surface index*** (type of surface, snowy background, presence of ice);
3) ***Event type index*** (snow storm, stratiform rain, convective cells);
4) ***Internal algorithm performance index*** (i.e., dependence on scan viewing angle).

The quality index and the PCI are connected as shown in **Table 08**:

Table 08: Quality index values and interpretation and correspondence with percentage of confidence index (PCI).

Percentage of confidence index	Quality flag	Quality index
0	Missing data	0
1-20	Poor	1
21-80	Fair	2
81-100	Good	3

The PCI evaluation procedure is based on the following steps:

1) A preliminary PCI value is assigned with different criteria depending on the output of the screening procedure:

a. For no-rain pixels a preliminary value of PCI is evaluated according to some conditions on the $TB^{max}_{53.6}$ (defined in the screening module) provided in **Table 09**. The presence of snow/ice on the background surface lowers the value of the PCI which is limited to 10.

Table 09: Preliminary PCI thresholds based on screening algorithm.

Test on TB	Environmental situation	Preliminary PCI
$TB_{53.6} < 242$ K	very cold/dry (not precipitating)	0
$TB_{53.6} >= 242$ K & $TB_{53.6} < 248$ K	cold/dry situation	20
$TB_{53.6} >= 248$ K	warm/wet situation	50

b. For rainy pixels the PCI value is based on a procedure that identifies the type of observed event. This procedure (Funatsu et al., 2007, 2012) classifies 4 typologies of precipitation: not identified/light stratiform, stratiform, convective, heavy convective (overshooting top) and associates a preliminary value of PCI according to the values listed in **Table 10**. Also in this case, the presence of snowy/iced background on area with precipitation lowers the value of the PCI (the PCI value is limited to 10). The preliminary PCI value associated to precipitation on coastal area has an upper limit equal to 30 (quality flag "fair").

Table 10: Preliminary PCI based on precipitation type

Typology of event	Preliminary PCI
not identified/light stratiform	40
stratiform	50
convective	90
heavy convective	90

2) The preliminary PCI value is combined to some correction coefficients to become the final value of PCI:

a. satellite operation status coefficient (the PCI value decreases when satellite has some problem, i.e. damaged channels, etc.);
b. scan geometry coefficient (the PCI value decreases as the scan viewing angle increases);
c. data quality coefficient (the PCI is set to 0 in case of corrupted channels and/or unrealistic values of measured TBs).

3.3.10 Algorithm validation/heritage

P-IN-MHS is the extended version of the product for H-SAF Area to provide rainfall rate estimates for the MSG area correspondent to LAT 60°S - 75°N, LON 60°W - 60°E [1]. The product has been optimized for Europe and Mediterranean area (H SAF area) and for Africa and Southern Atlantic. H02B is designed to provide the same rainfall estimates over the H SAF area as those previously provided (ver. 2.7). The previous versions of the P-IN-MHS product were based on the algorithm of Surussavadee and Staelin (2008a, b), consisting of an artificial neural network (ANN) based precipitation retrieval algorithm for applications with measurements from AMSU-A and AMSU-B/MHS (AMSU-B is MHS's ancestor instrument on an earlier generation of NOAA POES satellites). They trained their algorithm through a database generated from cloud-radiation model (CRM) precipitation simulations. They used as their CRM basis, the Pennsylvania State University / National Center for Atmospheric Research (PSU/NCAR) Mesoscale Model-5 (MM5) described by Dudhia (1993) and Grell et al. (1994), with which they produced multiple simulations at a number of locations on the globe. Their algorithm includes particular corrections for limb-sounding effects, due to cross-track scanning, resolution enhancement techniques for AMSU-A data and techniques for precipitation screening purposes that are based on principal component analysis.

During the development of the product the performance of P-IN-MHS has been tested over Africa and Southern Atlantic using a two year dataset (2011-2013) of coincident overpasses with TRMM PR. The goal of the verification analysis (not to be considered as a validation activity) was to better understand how the algorithm performs when applied to specific typology of meteorological events and over different backgrounds. In order to do this, TRMM PR measurements are used as reference, providing a uniform (a single instrument for the whole verification analysis) rain rate estimation even if with some limitations and covering only +/- 35 deg Lat. The choice to use the TRMM PR is also linked to the lack or scarcity of other available instruments (radar or rain gauge) over Africa and Southern Atlantic area.

Over the H SAF area P-IN-MHS is found to perform reasonably well over sea and vegetated land for all types of precipitation as evaluated against radar and raingauge data. The algorithms also work over land with snow and sea ice, but with a strong risk of false detections. See Panegrossi et al. (2013) for further details and results on validation study over Europe. Detailed report of the product validation activity for product P-IN-MHS over H SAF area is provided as document:

- PVR-02: Product Validation Report for H02B.

Over Africa and Southern Atlantic the performance are good over all types of surfaces. A verification study against two years (2011-2012) of coincident overpasses with TRMM PR has provided RMSE between 1.91 mm/h (desert) and 2.21 mm/h (land), CC between 0.58 (desert) and 0.78 (coast). Low false alarm over desert (39%) has been a major achievement mostly due to the new CCA methodology for screening not-precipitating pixels. See Panegrossi et al. (2014) for further details and results on validation study over Africa.

The major achievements made with P-IN-MHS with respect to the former versions are: 1) the consistency of the precipitation estimates and screening with respect to P-IN-SSMIS; 2) the retrieval of the phase of the precipitation; 3) the correction of the corrupt AMSU-A channel on board MetOp-A to be able to use this sensor. Another major improvement, which will have substantial effects on the validation results, is the determination of a pixel based quality index to be associated to the precipitation retrieval.

[1] It is noted that throughout this document the statement "full disc" is used in some cases as a simplified indication of the overall applicability of the product.

4 Examples of P-IN-MHS product

Figure 14 shows an example of MHS measurements at 157 GHz, and the corresponding P-IN-MHS rainfall rate map. **Figure 15** presents a detail of the rainfall rate map over African area with the associated map of the percentage of confidence index (PCI).

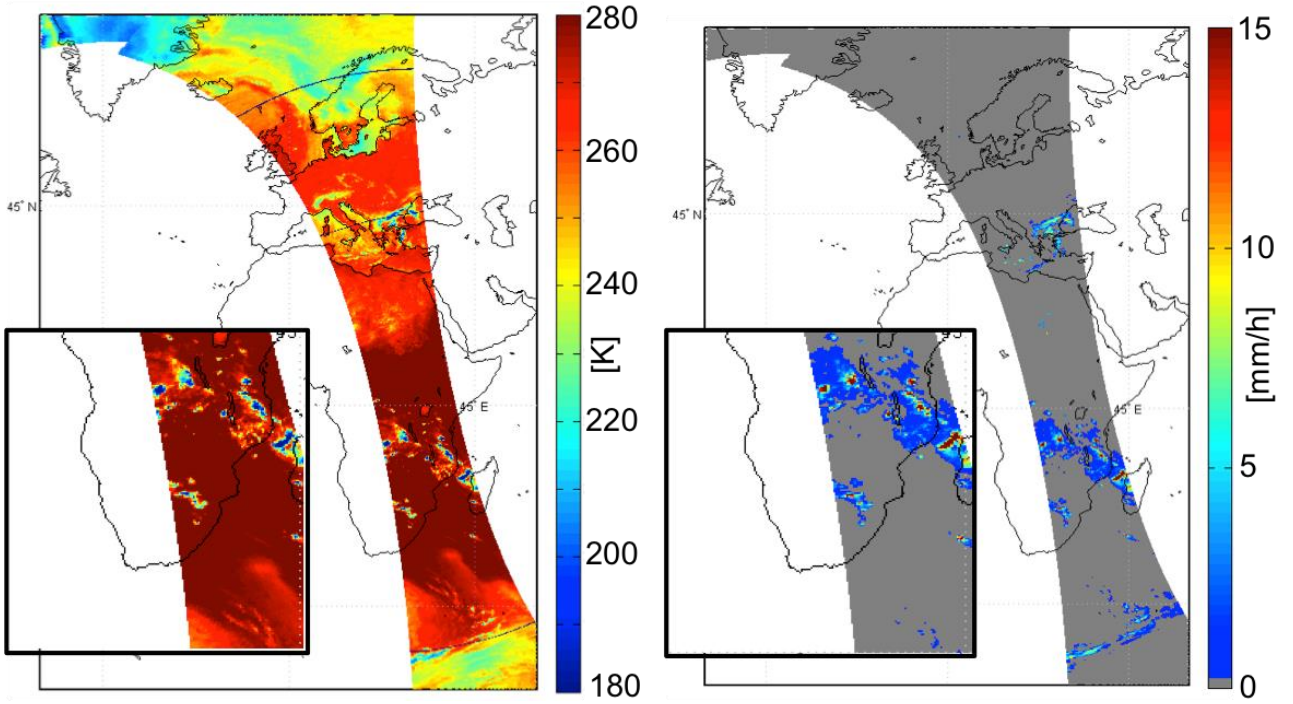

Fig. 14 - Example of a 157 GHz image for MHS orbit over the MSG area* LAT 60°S - 75°N, LON 60°W - 60°E *(left panel) and P-IN-MHS rainfall rate (mm/h) (right panel) - MetOp-A - 06 January 2012, 18:09 UTC

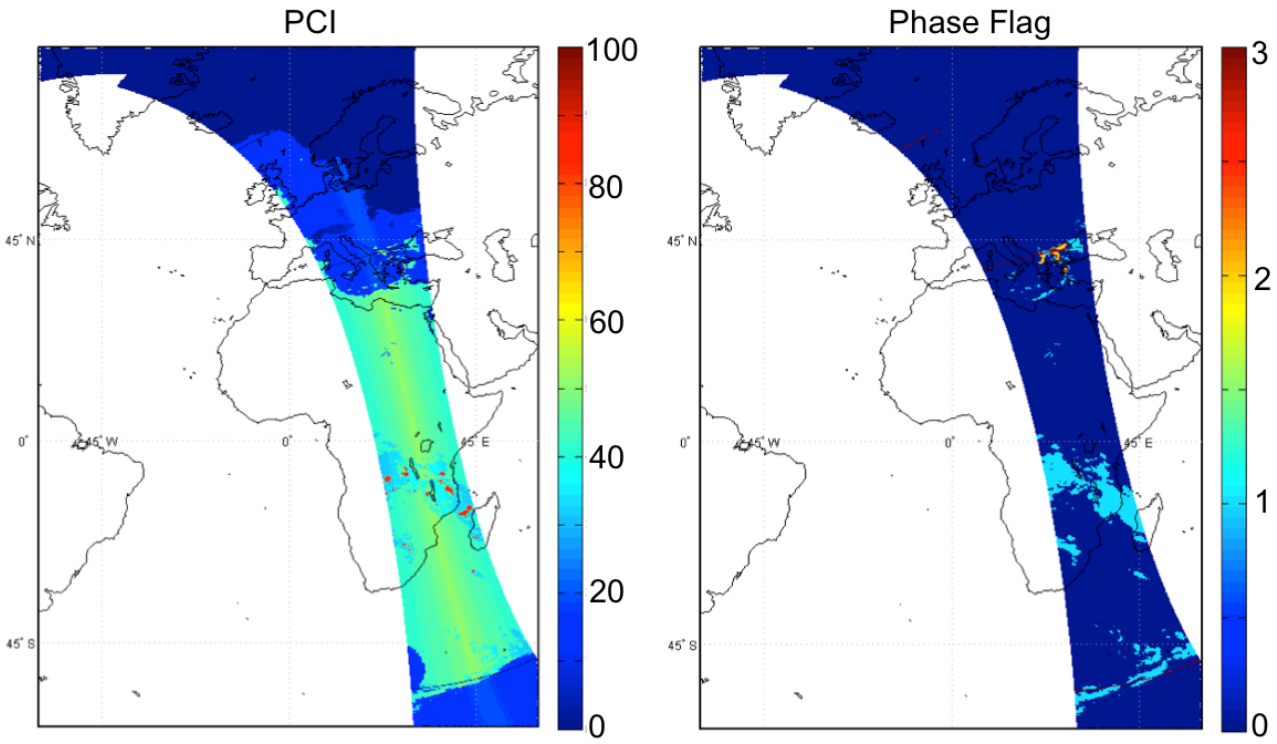

Fig. 15 – Example of P-IN-MHS PCI (left panel) and Phase flag (right panel) [0 no data, 1 liquid, 2 solid, 3 mixed]- MetOp-A - 06 January 2012, 18:09 UTC

5 References

AMSU-A: Advanced Microwave Sounding Unit-A (AMSU-A), in: NOAA KLM User's Guide, Section 3.3, NOAA National Environmental and Data Information Service, National Climatic Data Center, [http://www.ncdc.noaa.gov/oa/pod-guide/ncdc/docs/klm/cover.htm], 2009.

Anders, U. and Korn, O. "Model selection in neural networks", Neural Netw., 12, 309-323, 1999.

Bauer, P., E. Moreau, F. Chevallier, and U. O'Keeffe, "Multiple-scattering microwave radiative transfer for data assimilation applications," *Q. J. Roy. Meteor. Soc.,* vol. 132, pp. 1259-1281, Apr 2006.

Bennartz, R.: Optimal convolution of MHS to AMSU-A, J. Atmos. Oceanic Tech., 17, 1215-1225, 2000.

Casella, D., Panegrossi, G., Sanò, P., Mugnai, A., Smith, E.A., Tripoli, G.J., Dietrich, S., Formenton, M., Di Paola, F., Leung, H. W.-Y., and Mehta, A.V.: Transitioning from CRD to CDRD in Bayesian retrieval of rainfall from satellite passive microwave measurements, Part 2: Overcoming database profile selection ambiguity by consideration of meteorological control on microphysics, IEEE Trans. Geosci. Remote Sens., vol.51, no.9, 4650-4671, doi: 10.1109/T

GRS.2013.2258161, 2013

Casella, D., Panegrossi, G., Sanò, P., Milani, L., Petracca, M., and Dietrich, S.: A novelalgorithm for detection of precipitation in tropicalregionsusing PMW radiometers, Atmos. Meas. Tech., 8, 1217-1232, doi:10.5194/amt-8-1217-2015, 2015.

Chen F.W. and D.H. Staelin, 2001: "Millimeter-Wave Observations of Precipitation Using AMSU on the NOAA-15 Satellite". *Proc. of the 2001 IEEE InternationalGeoscience and Remote Sensing Symposium*, 9-13 July 2001, vol. 3, pp. 1044-1045.

Chen F.W. and D.H. Staelin, 2002: "Millimeter-wave observation of precipitation using AMSU on the NOAA-15 satellite". *Proc. of the 2002 Int. Geoscience and Remote Sensing Symposium*, Toronto, 24-28 June 2002, vol. 1, 460-462.

Chen F.W. and D.H. Staelin, 2003: "AIRS/AMSU/HSB Precipitation Estimates". *IEEE Transactions on Geoscience and Remote Sensing*, vol. 41, no. 2, pp. 410-417.

Chen F.W., 2004: "Global Estimation of Precipitation Using Opaque Microwave Bands". Ph.D. thesis, MIT.

Cotton W.R., G.J. Tripoli, R.M. Rauber and E.A. Mulvihill, 1986: "Numerical Simulation of the effects of varying ice crystal nucleation rate and aggregation processes on orographic snowfall". *J. Clim. Apl. Meteor.***25:** 1658-1680.

Cotton W.R., M.A. Stephens, T. Nehrkorn and G.J. Tripoli, 1982: "The Colorado State University three-dimensional cloud/mesoscale model-1982. Part II: An ice phase parameterization". *J. Res. Atmos.***16:** 295-320.

Deirmendjian D., 1969: "*Electromagnetic Scattering on Spherical Polydispersions*". American Elsevier Publishing Co., New York, NY.

Dudhia, J.: A nonhydrostatic version of the Penn State-NCAR Mesoscale Model: Validation tests and simulation of an Atlantic cyclone and cold front, Mon. Wea. Rev., 121, 1493-1513, 1993.

Flatau P., G.J. Tripoli, J. Berlinde and W. Cotton, 1989: "The CSU RAMS Cloud Microphysics Module: General Theory and Code Documentation". *Technical Report 451*, Colorado State University, 88 pp.

Funatsu, B. M., V. Dubreuil, C. Claud, D. Arvor, and M. A. Gan (2012), Convective activity in MatoGrosso state (Brazil) from microwave satellite observations: Comparisons between AMSU and TRMM data sets, J. Geophys. Res., 117, D16109, doi:10.1029/2011JD017259

Funatsu, B. M., C. Claud, and J.-P. Chaboureau (2007), Potential of Advanced Microwave Sounding Unit to identify precipitating systems and associated upper-level features in the Mediterranean region: Case studies, J. Geophys. Res., 112, D17113, doi:10.1029/2006JD008297

Gasiewski A.J., 1988: "Atmospheric Temperature Sounding and Precipitation Cell Parameter Estimation Using Passive 118-GHz O2 Observations". Ph.D. thesis, Department of Electrical Engineering and Computer Science, MIT.

Gasiewski A.J., 1993: "Microwave Radiative Transfer in Hydrometeors". In *Atmospheric Remote Sensing by Microwave Radiometry* (edited by M.A. Janssen), John Wiley& Sons, Inc., New York, NY.

Goldberg M.D. and H.E. Fleming, 1995: "An Algorithm to Generate Deep-Layer Temperatures from Microwave Satellite Observations for the Purpose of Monitoring Climate Change". *Journal of Climate***8**: 993-1004.

Goldberg M.D., D.S. Crosby and L. Zhou, 2001: "The Limb Adjustment of AMSU A Observations: Methodology and validation". *Journal of Applied Meteorology*, 40, 70-83.

Grell, G., Dudhia, J., and Stauffer, D. R.: A Description of the Fifth Generation Penn State/NCAR Mesoscale Model (MM5), NCAR Techical Note NCAR/TN-398+STR, National Center for Atmospheric Research, Boulder, Colorado, USA, 121 pp., 1994.

Grenfell T.C. and S.G. Warren, 1999: "Representation of a nonspherical ice particle by a collection of independent spheres for scattering and absorption of radiation". *J. Geophys. Res.*, **104**, 31697-31709.

Groody N., F. Weng and R. Ferraro, Application of AMSU for obtaining hydrological parameters, Microwave Radiometry and Remote Sensing of the Earth's Surface and Atmosphere, P. Pampaloni, S. Paloscia , eds.: VSP, pp.339-352, 2000.

Hall D.L. and J. Llinas, 1997: "An Introduction to Multisensor Data Fusion". *Proc. of the 1997 IEEE*, vol. 85, no. 1, 6-23.

Haykin, S.O.: Neural Networks: A Comprehensive Foundation, 2nd Edition, Prentice Hall, 842 pp., 1998.

Haykin, S.O.: Neural Networks and Learning Machines, 3rd Edition. Prentice Hall, 906 pp., 2009.

Hewison T.J., 2001: "Airborne measurements of forest and agricultural land surface emissivity at millimeter wavelengths".*Geoscience and Remote Sensing*, IEEE Transactions, vol. 39, issue 2, 393- 400.

Hewison T.J. and S.J. English, 1999: **"**Airborne retrievals of snow and ice surface emissivity at millimeter wavelengths". *Geoscience and Remote Sensing*, IEEE Transactions.vol. 37, issue 4, 1871-1879.

Hewison, T. and S. English, 2000: "Fast models for land surface emissivity". In *Radiative Transfer Models for Microwave Radiometry* (C. Matzler, ed.), COST Action 712, Directorate-General for Research, European Commission, Brussels, Belgium, 117-127.

Hufford G., 1991: "A Model for the Complex Permittivity of Ice at Frequencies Below 1 THz". *International Journal of Infrared and Millimeter Waves*, Vol. 12, No. 7, 677-682.

Karkkainen K., A. Shivola and K. Nikoskinen, 2001 "Analysis of a three-dimensional dielectric misture with finite difference method". *IEEE Trans. Geosci. Remote. Sens* 39, 1013-1018.

Kedem B., H. Pavlopoulos, X. Guan and D.A. Short, 1994: "A Probability Distribution Model for Rain Rate". *Journal of Applied Meteorology*, vol. 33, no. 12, 1486-1493, Dec. 1994.

Kulie, M. S., R. Bennartz, T. J. Greenwald, Y. Chen, and F. Z. Weng, "Uncertainties in Microwave Properties of Frozen Precipitation Implications for Remote Sensing and Data Assimilation," *J. Atmos. Sci.,* vol. 67, pp. 3471-3487, Nov 2010

Lippmann R.P., 1987: "An Introduction to Computing with Neural Nets". *IEEE Acoustics, Speech, and Signal Processing Magazine*, vol. 4, no. 2, 4-22.

Liebe H.J. and G.G. Gimmestad, 1978: "Calculation of clear air EHF refractivity". *Radio Sci*., **13**, 245-251.

Liebe H.J., 1985: "An updated model for millimeter wave propagation in moist air". *Radio Sci*., **20**, 1069-1089.

Liou, K., *An Introduction to Atmospheric Radiation (2nd Edition)* vol. 84: Academic Press, 2002.

Liu Q., C. Simmer and E. Ruprecht, 1996: "Three-dimensional radiative transfer effects of clouds in the microwave spectral range". *J. Geophys. Res*., **101**, 4289-4298.

Marzban C. "Basic statistics and basic AI: neural networks, in: Artificial Intelligence Methods in the Environmental Science" edited by: Haupt, S.E., Pasini, A., and Marzban C., Springer, 15-47, 2009.

MHS: Advanced Microwave Sounding Unit-A (AMSU-A), NOAA KLM User's Guide, Section 3.3, NOAA National Environmental and Data Information Service, National Climatic Data Center, [http://www.ncdc.noaa.gov/oa/pod-guide/ncdc/docs/klm/cover.htm], 2009.

Mugnai A., D. Casella, E. Cattani, S. Dietrich, S. Laviola, V. Levizzani, G. Panegrossi, M. Petracca, P. Sanò, F. Di Paola, D. Biron, L. De Leonibus, D. Melfi, P. Rosci, A. Vocino, F. Zauli, S. Puca, A. Rinollo, L. Milani, F. Porcù, and F. Gattari: Precipitationproducts from the Hydrology SAF, Nat. Hazards Earth Syst. Sci., 13, 1959-1981, doi:10.5194/nhess-13-1959-2013, 2013a.

Mugnai A., E. A. Smith, G. J. Tripoli, B. Bizzarri, D. Casella, S. Dietrich, F. Di Paola, G. Panegrossi, P. Sanò, CDRD and PNPR Satellite Passive MicrowavePrecipitationRetrievalAlgorithms: EuroTRMM / EURAINSAT Origins and H SAF Operations, Nat. Hazards Earth Syst. Sci., 13, 887-912, doi:10.5194/nhess-13-887-2013, 2013b.

Panegrossi, G., Dietrich, S., Marzano, F.S., Mugnai, A., Smith, E.A., Xiang, X., Tripoli, G.J., Wang, P.K., and PoiaresBaptista, J.P.V.: Use of cloud model microphysics for passive microwave-based precipitation retrieval: Significance of consistency between model and measurement manifolds, J. Atmos. Sci., 55, 1644-1673, 1998.

Panegrossi, G., "Validation of Microphysics Parameterization in Cloud Resolving Models using Passive Microwave Measurements," Ph.D. Dissertation, Univ. of Wisconsin, Madison, WI, UW MET Publication No.04.00.P1, 2004.

Panegrossi G., Sanò P., D. Casella, S. Dietrich, M. Petracca, A. Mugnai, A verification study over Europe of AMSU-A/MHS and SSMIS passive microwave precipitation retrievals, Proc. 2013 EUMETSAT/AMS Meteorol. Sat. Conference, Vienna, Sept. 2013

Panegrossi G., Sanò P., D. Casella, S. Dietrich, L. Milani, M. Petracca, A. Mugnai,CDRD and PNPR passive microwave precipitation retrieval algorithms:extension to the MSG full disk area within H SAF,Proc. 2014 EUMETSAT/AMS Meteorol. Sat. Conference, Geneva, Sept. 2014

Pohl C. and J.L. van Genderen, 1998: "Multisensor Image Fusion in Remote Sensing: Concepts, Methods, and Application". International Journal of Remote Sensing, vol. 19, no. 5, pp. 823-854, 1998.

Prigent C, Aires F, Rossow WB. 2006. Land surface microwave emissivities over the globe for a decade. Bull. Am. Meteorol. Soc. 87: 1573–1584. DOI:10.1175/BAMS-87-11-1573.

Roberti L., J. Haferman and C. Kummerow, 1994: "Microwave radiative transfer through horizontally inhomogeneous precipitating clouds". J. Geophys. Res., **99**, 16707-16718.

Rosenkranz, P.: Rapid Radiative Transfer Model for AMSU/HSB Channels,IEEE Trans. Geosci. Rem. Sens., 41, 362-368, 2003.

Sanò, P., Casella, D., Mugnai, A., Schiavon, A., Smith, E.A., and Tripoli, G.J.: Transitioning from CRD to CDRD in Bayesian retrieval of rainfall from satellite passive microwave measurements, Part 1: Algorithm description and testing, IEEE Trans. Geosci. Remote Sens., Vol. 51, no. 7, 4119-4143, doi: 10.1109/TGRS.2012.2227332, 2013.

Sanò, P., Panegrossi, G., Casella, D., Di Paola, F., Milani, L., Mugnai, A., Petracca, M., and Dietrich, S.: The Passive microwaveNeural network PrecipitationRetrieval (PNPR) algorithm for AMSU/MHS observations: description and application to European case studies, Atmos. Meas. Tech., 8, 837-857, doi:10.5194/amt-8-837-2015, 2015.

Smith, E. A., P. Bauer, F. S. Marzano, C. D. Kummerow, D. McKague, A. Mugnai, and G. Panegrossi, "Intercomparison of microwave radiative transfer models for precipitating clouds," IEEE Trans. Geosci. Remote Sens, vol. 40, pp. 541-549, 2002.

Smith E.A., Hester W.-Y. Leung, James B. Elsner, Amita V. Mehta, Gregory J. Tripoli,Daniele Casella, Stefano Dietrich, Alberto Mugnai, Giulia Panegrossi, Paolo Sanò: Transitioning from CRD to CDRD in Bayesian Retrieval of Rainfall from Satellite Passive Microwave Measurements: Part 3. Identification of Optimal Meteorological Tags, Nat. Hazards Earth Syst. Sci., 13, 1185-1208, doi:10.5194/nhess-13-1185-2013, 2013.

Shivola A., 1989: "Self-Consistency Aspects of Dielectric Mixing Theories". *IEEE Trans. Geosci. Remote. Sens*. 27, 403-415.

Schlűssel P. and H. Luthardt, 1991, "Surface Wind Speeds Over the North Sea From Special Sensor Microwave/Imager Observations". *J. Geophys. Res*., vol. 96, No. C3, 4845-4853.

Spina M.S., M.J. Schwartz, D.H. Staelin and A.J. Gasiewski, 1998: "Application of Multilayer Feedforward Neural Networks to Precipitation Cell-Top Altitude Estimation". *IEEE Transactions on Geoscience and Remote Sensing*, vol. 36, no. 1, 154-162.

Staelin D.H, F.W. Chen and A. Fuentes, 1999: "Precipitation Measurements Using 183 GHz AMSU Satellite Observations". *Proc. of the 1999 IEEE International Geoscience and Remote Sensing Symposium*, vol. 4 , 2069-2071.

Staelin D.H. and F.W. Chen, 2000: "Precipitation Observations Near 54 and 183 GHz Using the NOAA-15 Satellite". *IEEE Transactions on Geoscience and Remote Sensing*, vol. 38, no. 5, 2322-2332.

Surussavadee C., 2006: "Passive Millimeter-Wave Retrieval of Global Precipitation Utilizing Satellites and a Numerical Weather Prediction Model". *Graduation thesis*, MIT Department of Electrical Engineering and Computer Science.

Surussavadee C. and D.H. Staelin, 2006: "Comparison of AMSU millimeterwave satellite observations, MM5/TBSCAT predicted radiances, and electromagnetic models for hydrometeors". *IEEE Trans. Geosci. Remote Sens.*, **44**, 2667-2678.

Surussavadee, C., and Staelin, D.H.: Global millimeter-wave precipitation retrievals trained with a cloud-resolving numerical weather prediction model, Part I: Retrieval design, IEEE Trans. Geosci. Remote Sens., 46, 99-108, 2008a.

Surussavadee, C., and Staelin, D.H.: Global millimeter-wave precipitation retrievals trained with a cloud-resolving numerical weather prediction model, Part II: Performance evaluation, IEEE Trans. Geosci. Remote Sens., 46, 109-118, 2008b.

Surussavadee, C, and David H. Staelin, 2009: Satellite retrievals of Arctic and Equatorial rain and snowfall rates using millimeters wavelengths, IEEE Trans. Geosci. Rem. Sens., 47, 3697-3707.

Tripoli G.J. and W.R. Cotton, 1981: "The use of ice-liquid water potential temperature as a thermodynamic variable in deep atmospheric models". *Mon. Wea. Rev.*, **109,** 1094-1102.

Tripoli G.J. and W.R. Cotton, 1982: "The Colorado State University three-dimensional cloud / mesoscale model-1982. Part I: General theoretical framework and sensitivity experiments". *J. Rech. Atmos*. **16:** 185-200.

Tripoli G.J. and W.R. Cotton, 1986: "An intense, quasi-steady thunderstorm over mountainous terrain, part IV: three-dimensional numerical simulation". *J. Atmos. Sci*., **43,** 894-912.

Tripoli G.J., 1992a: "A non-hydrostatic model designed to simulate scale interaction". *Mon. Wea. Rev.*, **120**, 1342-1359.

Tripoli G.J., 1992b: "An explicit three-dimensional non-hydrostatic numerical simulation of a tropical cyclone". *Meteor. Atmos. Phys.*, **49**, 229-254.

Tripoli G. J. and Smith E.A., 2014: "Introducing variable-step topography (VST) coordinates in dynamically constrained, scalable, nonhydrostatic atmospheric models: Review of rationale and solutions on classical obstacle flow calibration problems. ," *Dyn. Atmos. Oceans,* **66** (2014) 28-57.

Tsai V.J.D, 2003: "Frequency-Based Fusion of Multiresolution Images". *Proc. of the 2003 IEEE International Geoscience and Remote Sensing Symposium*, vol.6, 3665-3667.

Ulaby F.T., R.K. Moore and A.K. Fung, 1981: "*Microwave Remote Sensing: Active and Passive*", Addison-Wesley Pub. Co., Reading, MA.

Wald L., 1999: "Some Terms of Reference in Data Fusion". *IEEE Transactions on Geoscience and Remote Sensing*, vol. 37, no. 3, 1190-1193.

Wark D.Q., 1993: "Adjustment of TIROS operational vertical sounder data to a vertical view". *NOAA Tech. Rep. NESDIS-64*, 36 pp.

Annex 1: Introduction to H SAF

The EUMETSAT Satellite Application Facilities

H SAF is part of the distributed application ground segment of the "*European Organization for the Exploitation of Meteorological Satellites (EUMETSAT)*". The application ground segment consists of a "*Central Application Facilities*" located at EUMETSAT Headquarters, and a network of eight "*Satellite Application Facilities (SAFs)*", located and managed by EUMETSAT Member States and dedicated to development and operational activities to provide satellite-derived data to support specific user communities (see Figure 19):

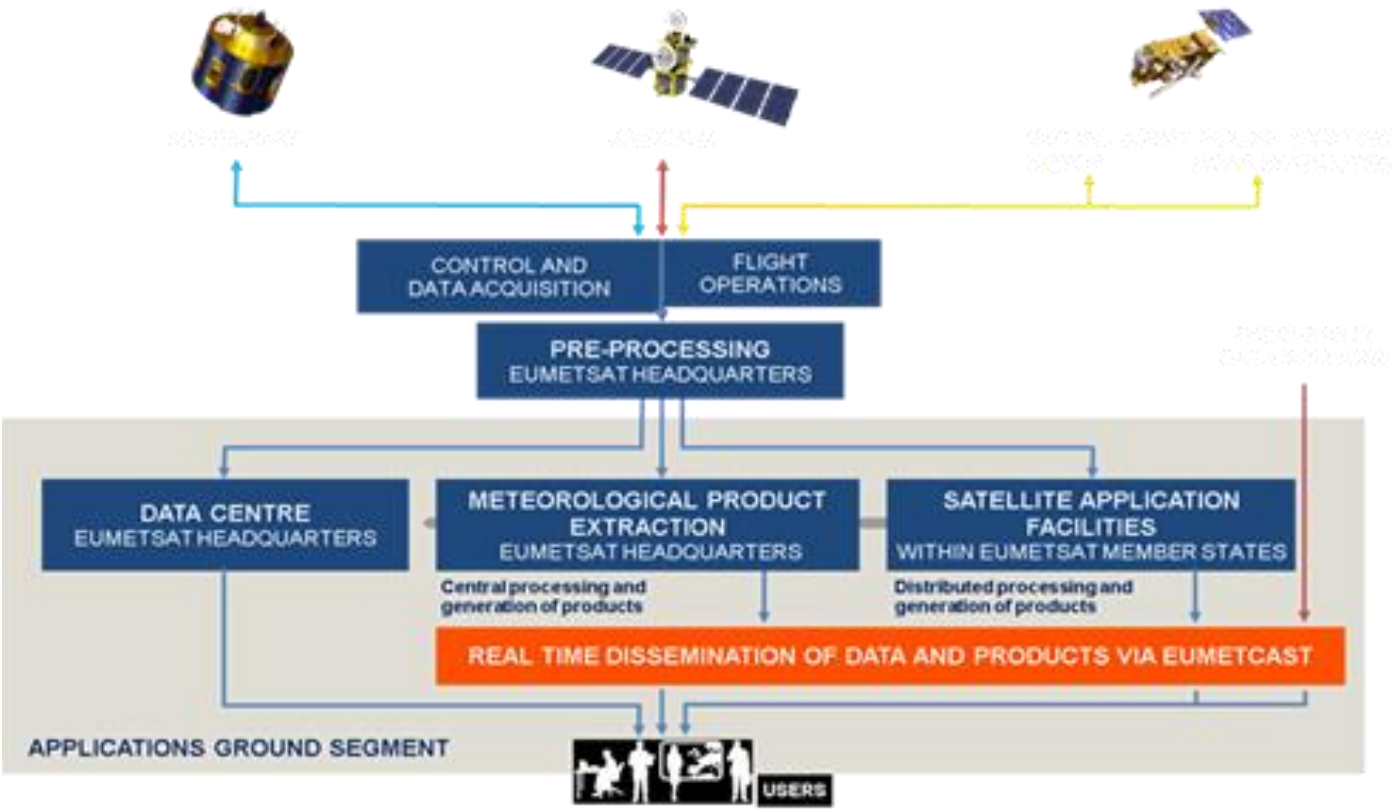

Figure 19: Conceptual scheme of the EUMETSAT Application Ground Segment

Figure 20 depicts the composition of the EUMETSAT SAF network, with the indication of each SAF's specific theme and Leading Entity.

Figure 20: Current composition of the EUMETSAT SAF Network

Purpose of the H SAF

The main objectives of H SAF are:

a. ***to provide new satellite-derived products*** from existing and future satellites with sufficient time and space resolution to satisfy the needs of operational hydrology, by generating, centralizing, archiving and disseminating the identified products:

- precipitation (liquid, solid, rate, accumulated);
- soil moisture (at large-scale, at local-scale, at surface, in the roots region);
- snow parameters (detection, cover, melting conditions, water equivalent);

b. ***to perform independent validation of the usefulness of the products*** for fighting against floods, landslides, avalanches, and evaluating water resources; the activity includes:

- downscaling/upscaling modelling from observed/predicted fields to basin level;
- fusion of satellite-derived measurements with data from radar and raingauge networks;
- assimilation of satellite-derived products in hydrological models;
- assessment of the impact of the new satellite-derived products on hydrological applications.

Products / Deliveries of the H SAF

For the full list of the Operational products delivered by H SAF, and for details on their characteristics, please see H SAF website hsaf.meteoam.it.
All products are available via EUMETSAT data delivery service (EUMETCast, http://www.eumetsat.int/website/home/Data/DataDelivery/EUMETCast/index.html), or via ftp download; they are also published in the H SAF website hsaf.meteoam.it.
All intellectual property rights of the H SAF products belong to EUMETSAT. The use of these products is granted to every interested user, free of charge. If you wish to use these products, EUMETSAT's copyright credit must be shown by displaying the words "copyright (year) EUMETSAT" on each of the products used.

System Overview

H SAF is led by the Italian Air Force Meteorological Service (ITAF MET) and carried on by a consortium of 21 members from 11 countries (see website: hsaf.meteoam.it for details)
Following major areas can be distinguished within the H SAF system context:

- Product generation area
- Central Services area (for data archiving, dissemination, catalogue and any other centralized services)
- Validation services area which includes Quality Monitoring/Assessment and Hydrological Impact Validation.

Products generation area is composed of 5 processing centres physically deployed in 5 different countries; these are:

- for precipitation products: ITAF COMET (Italy)
- for soil moisture products: ZAMG (Austria), ECMWF (UK)
- for snow products: TSMS (Turkey), FMI (Finland)

Central area provides systems for archiving and dissemination; located at ITAF COMET (Italy), it is interfaced with the production area through a front-end, in charge of product collecting.
A central archive is aimed to the maintenance of the H SAF products; it is also located at ITAF COMET.
Validation services provided by H SAF consists of:

- Hydrovalidation of the products using models (hydrological impact assessment);
- Product validation (Quality Assessment and Monitoring).

Both services are based on country-specific activities such as impact studies (for hydrological study) or product validation and value assessment.
Hydrovalidation service is coordinated by IMWM (Poland), whilst Quality Assessment and Monitoring service is coordinated by DPC (Italy): The Services' activities are performed by experts from the national meteorological and hydrological Institutes of Austria, Belgium, Bulgaria, Finland, France, Germany, Hungary, Italy, Poland, Slovakia, Turkey, and from ECMWF.

Annex 2: Acronyms

AMSU	Advanced Microwave Sounding Unit (on NOAA and MetOp)
AMSU-A	Advanced Microwave Sounding Unit - A (on NOAA and MetOp)
MHS	Advanced Microwave Sounding Unit - B (on NOAA up to 17)
ATBD	AlgorithmsTheoretical Baseline Document
AU	Anadolu University (in Turkey)
BfG	Bundesanstalt für Gewässerkunde (in Germany)
CAF	Central Application Facility (of EUMETSAT)
CDOP	Continuous Development-Operations Phase
CESBIO	Centre d'Etudes Spatiales de la BIOsphere (of CNRS, in France)
CM-SAF	SAF on Climate Monitoring
COMET	Centro Operativo per la Meteorologia (in Italy)
CNR	Consiglio Nazionale delle Ricerche (of Italy)
CNRS	Centre Nationale de la Recherche Scientifique (of France)
DMSP	Defense Meteorological Satellite Program
DPC	Dipartimento Protezione Civile (of Italy)
EARS	EUMETSAT Advanced Retransmission Service
ECMWF	European Centre for Medium-range Weather Forecasts
EDC	EUMETSAT Data Centre, previously known as U-MARF
EUM	Short for EUMETSAT
EUMETCast	EUMETSAT's Broadcast System for Environmental Data
EUMETSAT	European Organisation for the Exploitation of Meteorological Satellites
FMI	Finnish Meteorological Institute
FTP	File Transfer Protocol
GEO	Geostationary Earth Orbit
HDF	Hierarchical Data Format
HRV	High Resolution Visible (one SEVIRI channel)
H SAF	SAF on Support to Operational Hydrology and Water Management
IDL©	Interactive Data Language
IFOV	Instantaneous Field Of View
IMWM	Institute of Meteorology and Water Management (in Poland)
IPF	Institut für Photogrammetrie und Fernerkundung (of TU-Wien, in Austria)
IPWG	International Precipitation Working Group
IR	Infra Red
IRM	Institut Royal Météorologique (of Belgium) (alternative of RMI)
ISAC	Istituto di Scienze dell'Atmosfera e del Clima (of CNR, Italy)
ITU	İstanbulTechnical University (in Turkey)
LATMOS	Laboratoire Atmosphères, Milieux, Observations Spatiales (of CNRS, in France)
LEO	Low Earth Orbit

LSA-SAF	SAF on Land Surface Analysis
Météo France	National Meteorological Service of France
METU	Middle East Technical University (in Turkey)
MHS	Microwave Humidity Sounder (on NOAA 18 and 19, and on MetOp)
MSG	Meteosat Second Generation (Meteosat 8, 9, 10, 11)
MVIRI	Meteosat Visible and Infra Red Imager (on Meteosat up to 7)
MW	Micro Wave
NESDIS	National Environmental Satellite, Data and Information Services
NMA	National Meteorological Administration (of Romania)
NOAA	National Oceanic and Atmospheric Administration (Agency and satellite)
NWC-SAF	SAF in support to Nowcasting & Very Short Range Forecasting
NWP	Numerical Weather Prediction
NWP-SAF	SAF on Numerical Weather Prediction
O3M-SAF	SAF on Ozone and Atmospheric Chemistry Monitoring
OMSZ	Hungarian Meteorological Service
ORR	Operations Readiness Review
OSI-SAF	SAF on Ocean and Sea Ice
PDF	Probability Density Function
PEHRPP	Pilot Evaluation of High Resolution Precipitation Products
Pixel	Picture element
PMW	Passive Micro-Wave
PP	Project Plan
PR	Precipitation Radar (on TRMM)
PUM	Product User Manual
PVR	Product Validation Report
RMI	Royal Meteorological Institute (of Belgium) (alternative of IRM)
RR	Rain Rate
RU	Rapid Update
SAF	Satellite Application Facility
SEVIRI	Spinning Enhanced Visible and Infra-Red Imager (on Meteosat from 8 onwards)
SHMÚ	Slovak Hydro-Meteorological Institute
SSM/I	Special Sensor Microwave / Imager (on DMSP up to F-15)
SSMIS	Special Sensor Microwave Imager/Sounder (on DMSP starting with S-16)
SYKE	Suomen ympäristökeskus (Finnish Environment Institute)
T_{BB}	Equivalent Blackbody Temperature (used for IR)
TKK	Teknillinen korkeakoulu (Helsinki University of Technology)
TMI	TRMM Microwave Imager (on TRMM)
TRMM	Tropical Rainfall Measuring Mission UKMO
TSMS	Turkish State Meteorological Service

TU-Wien	Technische Universität Wien (in Austria)
U-MARF	Unified Meteorological Archive and Retrieval Facility
UniFe	University of Ferrara (in Italy)
URD	User Requirements Document
UTC	Universal Coordinated Time
VIS	Visible
ZAMG	Zentralanstalt für Meteorologie und Geodynamik (of Austria)